

Associated Production of Neutrino and Dark Fermion at Future Lepton Colliders

Shao-Feng Ge ^{*1,2}, Kai Ma ^{†3,4}, Xiao-Dong Ma ^{‡5,6,7}, and Jie Sheng ^{§1,2}

¹Tsung-Dao Lee Institute & School of Physics and Astronomy, Shanghai Jiao Tong University, Shanghai 200240, China

²Key Laboratory for Particle Astrophysics and Cosmology (MOE) & Shanghai Key Laboratory for Particle Physics and Cosmology, Shanghai Jiao Tong University, Shanghai 200240, China

³Department of Physics, Shaanxi University of Technology, Hanzhong 723000, Shaanxi, China

⁴Ministry of Education Key Laboratory for Nonequilibrium Synthesis and Modulation of Condensed Matter, Shaanxi Province Key Laboratory of Quantum Information and Quantum Optoelectronic Devices, School of Physics, Xi'an Jiaotong University, Xi'an 710049, China

⁵Key Laboratory of Atomic and Subatomic Structure and Quantum Control (MOE), Institute of Quantum Matter, South China Normal University, Guangzhou 510006, China

⁶Guangdong Provincial Key Laboratory of Nuclear Science, Institute of Quantum Matter, South China Normal University, Guangzhou 510006, China

⁷Guangdong-Hong Kong Joint Laboratory of Quantum Matter, Southern Nuclear Science Computing Center, South China Normal University, Guangzhou 510006, China

Abstract

Fermionic dark matter can be pairly produced and hence searched with missing energy at colliders. We extend such probe to the associated production of a neutrino and a dark sector fermion at the future e^+e^- colliders such as CEPC, FCC-ee, ILC, and CLIC. Two typical processes, the mono-photon and electron-positron pair productions associated with missing energy, can serve the purpose. While the mono-photon search prevails at CEPC, FCC-ee, and ILC, the $e^+e^- \not{E}_T$ channel has more significant contributions at CLIC with much higher collision energy \sqrt{s} . The beam polarizations can help further suppressing the SM backgrounds to enhance the signal significance while differential cross sections can distinguish the Lorentz structure of various effective operators. The combined sensitivity can reach well above 1 TeV at CEPC/FCC-ee and ILC while it further touches 30 TeV at CLIC. Comparing with the updated results from the direct detection experiments (XENON1T, PandaX-II, PandaX-4T, LZ, and XENONnT), astrophysical X/γ -ray observations, and cosmological constraints for the sub-MeV absorption dark matter, the collider searches are actually more sensitive and hence can provide a complementary approach to addressing the dark fermions.

^{*}gesf@sjtu.edu.cn

[†]makai@ucas.ac.cn

[‡]maxid@scnu.edu.cn

[§]shengjie04@sjtu.edu.cn

1. Introduction

The existence of dark matter (DM) has been established by various cosmological and astrophysical observations [1–3]. However, its identity and physical properties are still unknown. We need more observational clues for the DM model building [4]. In addition to the cosmological searches [5], there are mainly three types of DM searches: direct detection [6–8], indirect detection [9–11], and collider search [12–15], to constrain the couplings between the DM and SM particles [4, 16, 17]. Most of them are given on the DM coupling with nucleons and hence effectively quarks. Note that colliders probe not just the true DM particle that survives until today but also any dark sector particles that can be directly generated as long as it is kinematically allowed. However, no clear evidence has been observed yet and hence puts strong constraints.

So it seems promising for DM to have leptophilic interactions. For instance, if the DM only directly couples with leptons, its coupling with quarks is then suppressed. Such leptophilic scenarios are characterized by a conspicuous gamma-ray in the galactic halo because of the radiatively induced annihilation rate into leptons and photons [18–21]. One particularly interesting possibility is the sterile neutrino DM that can produce astrophysical X -ray [22–27]. The leptophilic DM models have been discussed extensively in literature [28–46] and have the potential of explaining various experimental anomalies [47–49].

The collider search provides a tunable environment to distinguish the leptophilic and hadrophilic natures of DM. While hadron colliders mainly probe quark couplings [50–54], lepton colliders are more sensitive to the leptonic ones [47–49, 55–60]. Typically, the DM search at lepton collider utilizes the missing energy or momentum as characteristic signature, such as the mono-photon [61–66] and mono- Z [67–70] signals that have been studied extensively. In both cases, the associated production of a single bosonic DM or a pair of fermionic DM particles carries away missing energy [71–74]. This does not exhaust all the possibilities.

In addition to DM that survives in the Universe, neutrino and other dark fermions can also carry away some missing energy. It is natural to explore the possible associated production of dark fermion χ and neutrino ν . This coincides with the fermionic DM absorption on electron target, $\chi e \rightarrow \nu e$ in the sub-MeV mass range. Putting both electron legs to the initial state, a single dark fermion can also appear in the final state from the e^+e^- annihilation at lepton colliders. For instance, the process $e^+e^- \rightarrow \chi\nu$ can happen as long as the collision energy $\sqrt{s} > m_\chi$. One may also expect such collider searches to provide complementary constraints on the same operator as explored in the direct detection at least in the sub-MeV mass range. For the remaining mass range above MeV, the future lepton colliders serves as unique probe of other dark fermions.

The rest of this paper is organized as follows. In Sec. 2, we summarize the profound motiva-

tion and essential features of the fermionic absorption DM on electron target. The next Sec. 3 studies the mono-photon production at the future e^+e^- colliders with both polarized and unpolarized beams to obtain the expected exclusion limits at collision energies of 240 GeV, 500 GeV, and 3 TeV for CEPC/FCC-ee, ILC, and CLIC, respectively. We notice that the $e^+e^- \not{E}_T$ signal provides better sensitivity at higher energies as elaborated in Sec. 4. In Sec. 5, we provide the updated constraints from the DM overproduction, the astrophysical X/γ -ray observations, and the direct detection experiments for the sub-MeV fermionic absorption DM. The fully combined results and our conclusions can be found in Sec. 6.

2. Fermionic DM Absorption on Electron Target

The direct detection of DM employs nuclear recoil to manifest the existence of DM. Typically, a DM particle transfers part of its kinetic energy to the target nuclei via elastic scattering. Since the DM velocity has fixed distribution by the gravitational potential in our Milky Way Galaxy, the momentum transfer scales with the DM mass squared. Using heavy nuclei as target, the direct detection experiment is intrinsically sensitive to the weak scale DM particles. In addition, the energy threshold of direct detection experiments also limits the sensitivity for light DM candidates.

These difficulties can be overcome if DM converts its mass into recoil energies through the absorption process, such as $\chi e \rightarrow \nu e$ for fermionic DM χ . Since the final-state neutrino is almost massless, the DM mass is fully released. The aforementioned two problems, recoil energy scales with DM mass squared and the sensitivity is limited by the experimental energy threshold, can be evaded simultaneously. Such direct detection process can appear in a variant way at lepton colliders by moving the two electron legs to the initial state, $e^+e^- \rightarrow \chi\bar{\nu}$ or $\bar{\chi}\nu$, as we elaborate in this paper. More generally, the collider search covers not just the genuine DM particle that survives until today but also other dark fermions. In addition to being complementary, the collider search has its own advantage of exploring the whole dark sector.

Since the momentum transfer for the direct detection process is typically small, it is enough to use effective operators when exploring sensitivities there [75]. In effective field theory (EFT), operators are usually constructed according to the SM $SU(3)_c \times SU(2)_L \times U(1)_Y$ gauge symmetries. However, the weak symmetry $SU(2)_L$ should have already been broken at low energy and only the electromagnetic $U(1)_{\text{em}}$ symmetry remains to constrain the form of effective operators. The $\chi e \rightarrow \nu e$ and $e^+e^- \rightarrow \chi\bar{\nu}$ or $\bar{\chi}\nu$ process involves four fermions in the external states and

hence can be described by dimension-6 (dim-6) four-fermion effective operators,

$$\begin{aligned}
\mathcal{O}_S &\equiv (\bar{e}e) (\bar{\nu}_L \chi_R) , \\
\mathcal{O}_P &\equiv (\bar{e}i\gamma_5 e) (\bar{\nu}_L \chi_R) , \\
\mathcal{O}_V &\equiv (\bar{e}\gamma_\mu e) (\bar{\nu}_L \gamma^\mu \chi_L) , \\
\mathcal{O}_A &\equiv (\bar{e}\gamma_\mu \gamma_5 e) (\bar{\nu}_L \gamma^\mu \chi_L) , \\
\mathcal{O}_T &\equiv (\bar{e}\sigma_{\mu\nu} e) (\bar{\nu}_L \sigma^{\mu\nu} \chi_R) ,
\end{aligned} \tag{2.1}$$

as well as their hermitian conjugates [75]. The above parameterization is complete by including all the five independent Lorentz structures for the electron bilinear. Any other dim-6 operator can be expressed as a linear combination of these 5 operators via Dirac γ matrix identities and Fierz transformations [76–78]. The neutrino is assumed to be left-handed while the dark fermion χ is a Dirac fermion which has both left- and right-handed components. In the effective Lagrangian,

$$\mathcal{L}_{\text{eff}} = \sum_i \frac{1}{\Lambda_i^2} \mathcal{O}_i + \text{h.c.}, \tag{2.2}$$

each operator has a corresponding cut-off scale Λ_i that is related to possible fundamental physics. Although these absorption operators are originally established for the fermionic absorption DM, they also apply for any other dark fermion like sterile neutrino. We keep “*absorption*” in the name just as a reminder.

For collider searches, the EFT can still work as long as the cut-off scale Λ_i is higher than the collision energy. As explored at PandaX-4T, the existing data can already constrain the cut-off scale to be above 1 TeV [79]. It is safe to follow the EFT approach for future lepton colliders, such as CEPC/FCC-ee at $\sqrt{s} = 240$ GeV and ILC at 500 GeV, respectively. Even for CLIC with $\sqrt{s} = 3$ TeV, the EFT approach can still work with even higher reach of the probed scale, typically $\Lambda_i \sim \mathcal{O}(10)$ TeV.

3. Mono-Photon Production

Observing the mono-photon radiation is one of the most effective approach to search for dark particles at colliders [48, 61–63, 65–70, 80]. Missing energy and momentum are carried away by dark particles while the photon energy is observable. If the invisible particle is a single bosonic dark particle, the mono-photon is actually mono-energetic. Otherwise, the mono-photon has continuous spectrum. We consider possible test of a dark fermion at lepton colliders in the associated production with a neutrino. In contrast to the DM pair $\chi\bar{\chi}$ production as usually studied (for instance in [48]), the effective operators in Eq. (2.1) will induce events containing a single dark fermion χ (or $\bar{\chi}$) and an associated anti-neutrino $\bar{\nu}$ (or a neutrino ν), as shown in Fig. 1(a). Both dark fermion χ and neutrino can carry missing energy and momentum.

For heavy dark fermion, the decay width of $\chi \rightarrow \nu e^+ e^-$ can be large. So it is possible for the

dark fermion be partially visible. Detecting the decay process can provide stronger constraint with extra information. To be conservative, we only consider an invisible dark fermion with missing energy.

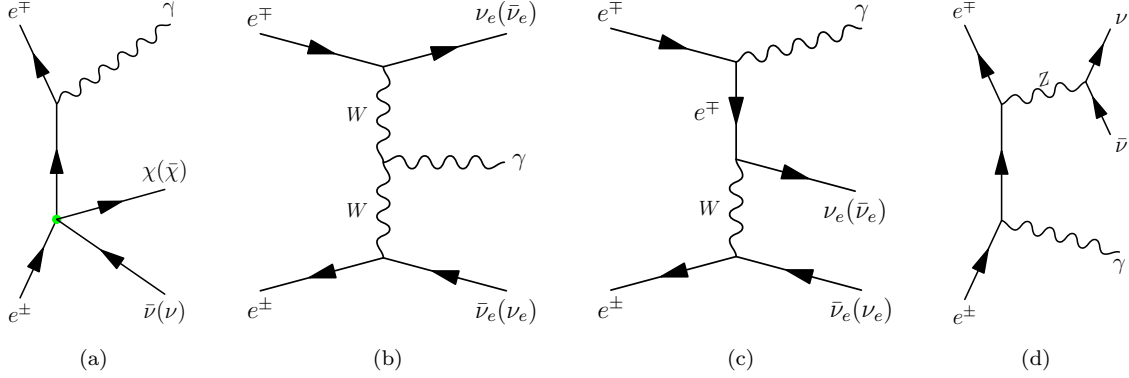


Fig. 1: The Feynman diagrams of the mono-photon production with e^+e^- collision, for signal (a) as well as the semi-irreducible backgrounds from the W mediated charged current (b)+(c) and Z resonant (d) channels.

3.1. Signal

Two subprocesses, $e^+e^- \rightarrow \gamma\chi\bar{\nu}$ and $e^+e^- \rightarrow \gamma\bar{\chi}\nu$ by exchanging a t -channel electron in the first Feynman diagram of Fig. 1, can contribute to the signal. In the massless limit for the incoming e^\pm beams, the differential polarized cross sections $\sigma_{\lambda_e-\lambda_{e^+}}$ summed over the two subprocesses are,

$$\frac{d\sigma_{\pm\pm}^{S,P}}{dm_X^2 d\cos\theta_\gamma} = \frac{1}{32\pi^3\Lambda^4} \frac{(m_X^2 - m_\chi^2)^2 (s^2 + m_X^4)}{s^2 (s - m_X^2) m_X^2 \sin^2\theta_\gamma}, \quad (3.1a)$$

$$\frac{d\sigma_{\pm\mp}^{V,A}}{dm_X^2 d\cos\theta_\gamma} = \frac{1}{384\pi^3\Lambda^4} \frac{(m_X^2 - m_\chi^2)^2 (2m_X^2 + m_\chi^2) s}{(s - m_X^2) m_X^6 \sin^2\theta_\gamma} (f_{V,A} + g_{V,A} \cos\theta_\gamma), \quad (3.1b)$$

$$\frac{d\sigma_{\pm\pm}^T}{dm_X^2 d\cos\theta_\gamma} = \frac{1}{768\pi^3\Lambda^4} \frac{(m_X^2 - m_\chi^2)^2 (m_X^2 + 2m_\chi^2) s^2}{(s - m_X^2) m_X^8 \sin^2\theta_\gamma} (f_T + g_T \cos\theta_\gamma), \quad (3.1c)$$

where $\lambda_{e^\pm} = \pm 1$ are the electron and positron helicities. Since neither the dark fermion χ nor the SM neutrino ν are detectable at lepton colliders, it makes no difference to treat the $\chi\nu$ system altogether as a single particle with missing invariant mass $m_X^2 \equiv (p_\nu + p_\chi)^2$. For convenience, we have defined functions $f_{V,A,T}$ and $g_{V,A,T}$,

$$f_{V,A} \equiv 1 + 2z_X + 10z_X^2 + 2z_X^3 + z_X^4, \quad (3.2a)$$

$$g_{V,A} \equiv (1 - z_X)^2 (1 + 4z_X + z_X^2), \quad (3.2b)$$

$$f_T \equiv 17 - 4z_X + 7z_X^2 + 56z_X^3 + 55z_X^4 - 4z_X^5 + z_X^6, \quad (3.2c)$$

$$g_T \equiv (1 - z_X)^3 (15 + 33z_X + 15z_X^2 + z_X^3), \quad (3.2d)$$

in terms of $z_X \equiv m_X^2/s$. Besides m_X , the only internal property of the $\chi\nu$ system that appears is the dark fermion mass m_χ while the parameter from the photon side is its scattering angle

θ_γ . For the scalar and pseudo-scalar operators, the situation is much simpler.

In the massless limit for electrons, which is an excellent approximation at high energy colliders, the cross section vanishes for the (pseudo-)scalar and tensor operators with the helicity combinations $\lambda_{e^-} = -\lambda_{e^+}$, and for the (axial-)vector operator with $\lambda_{e^-} = \lambda_{e^+}$. Since the associated photon in Fig. 1(a) arises from the initial state radiation (ISR), the cross sections exhibit a singular behavior at the colinear limit $\sin \theta_\gamma = 0$ which explains the $1/\sin^2 \theta_\gamma$ factor in Eq. (3.1). Although this divergent behavior can be regularized by the electron mass, it captures the correct feature in the forward and backward regions. Furthermore, signals are also singular if the emitted photon is very soft (when $m_X^2 \rightarrow s$) as summarized by the factor $1/(s - m_X^2)$. Considering this, our numerical calculations adopts the following kinematic cuts to enhance the simulation efficiency [58],

$$4^\circ < \theta_\gamma < 176^\circ \quad (|\eta_\gamma| < 3.35), \quad \text{and} \quad p_{T,\gamma} > 1 \text{ GeV}. \quad (3.3)$$

Our numerical simulations are conducted in **MadGraph5** [81] with model files generated by **FeynRules** [82].

The left panel of Fig. 2 shows the collision energy \sqrt{s} dependence of the total cross sections with the kinematic cuts given in Eq. (3.3). For illustration, signals are simulated with massless DM particle ($m_\chi = 0 \text{ GeV}$) and $\Lambda = 1 \text{ TeV}$. One can see that all the signal cross sections grow with \sqrt{s} . Contributions of the vector (blue dash-dotted) and axial vector (yellow long-dashed) operators are slightly larger than the scalar (red dotted) and pseudo-scalar (green dashed) ones while the tensor operator (cyan long-dash-dotted) has the smallest cross section. It is interesting to observe that there is no difference between the vector and axial-vector or between the scalar and pseudo-scalar operators. The right panel shows the normalized distribution as function of the photon polar angle θ_γ in the lab frame with a collision energy $\sqrt{s} = 500 \text{ GeV}$. As expected, for all the five effective operators, signals are significantly populated in the forward and backward regions with nearly indistinguishable polar angle distributions.

3.2. Background

The dominant background is the radiative neutrino pair production, *i.e.*, neutrino pair production together with a photon, as shown in Fig. 1(b), Fig. 1(c), and Fig. 1(d). Although the background does not share exactly the same final-state fermions with signal, neither neutrino nor dark matter is detectable at collider and hence we call such background as semi-irreducible. Note that other background diagrams with the SM Higgs boson are negligible since the electron Yukawa coupling is quite tiny. From the left panel of Fig. 2, one can see that at $\sqrt{s} = 1 \text{ TeV}$, the signals are about 1 order smaller than the semi-irreducible background (black-solid curve). Furthermore, the associated photon is emitted via ISR and hence the corresponding amplitude is singular when approaching $\sin \theta_\gamma = 0$. Consequently, both signals and the semi-irreducible background favor the forward and backward regions, as shown in the right panel of Fig. 2.

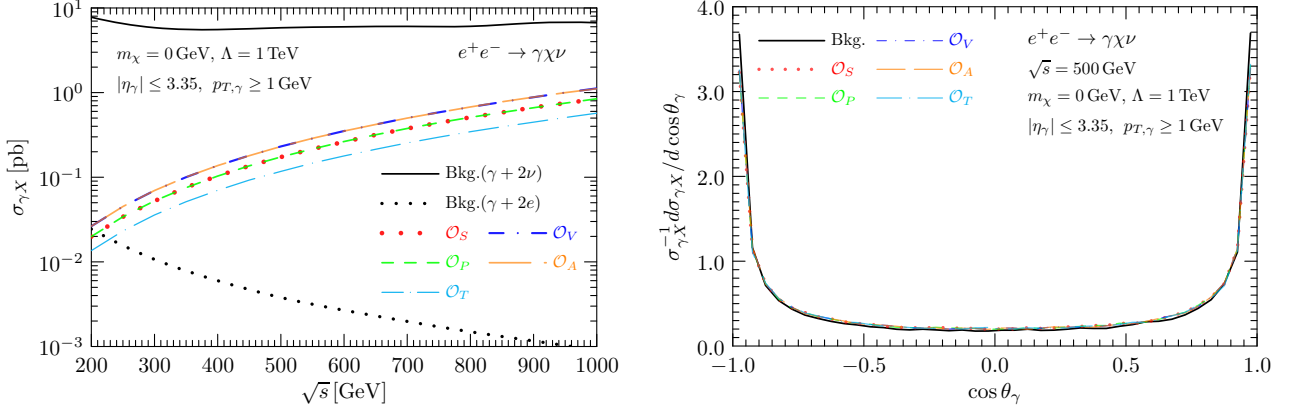


Fig. 2: **Left panel:** the mono-photon production cross sections as function of the collision energy \sqrt{s} . The signal ones (colorful non-solid curves) are obtained with vanishing dark fermion mass $m_\chi = 0$ GeV and cut-off scale $\Lambda_i = 1$ TeV. The background includes the semi-irreducible $e^+e^- \rightarrow \gamma + 2\nu$ (black-solid line) and the reducible one from the radiative Bhabha scattering $e^+e^- \rightarrow e^+e^- + 2\nu$ (black-dotted line). **Right panel:** the normalized photon polar angle (θ_γ) distributions in the lab frame with collider energy $\sqrt{s} = 500$ GeV. The kinematic cuts $p_{T,\gamma} < 1$ GeV and $|\eta_\gamma| < 3.35$ are in place.

Since photon is the only detectable particle for the signal, a mono- γ production with any other undetected particles can also contribute to the total background. The major contribution comes from the radiative Bhabha scattering ($e^+e^- \rightarrow \gamma e^+e^-$) of which the final-state e^+e^- evade detection in the very forward region [55]. Such Bhabha scattering has huge cross section and hence can potentially give a sizable contribution as reducible background. Note that the divergent configurations for the radiative Bhabha scattering should be removed at the generator level [58, 83, 84] following the treatments in [85],

$$m(e_{\text{in}}^\pm, e_{\text{out}}^\pm) < -1 \text{ GeV}, \quad m(e_{\text{out}}^-, e_{\text{out}}^+) > 1 \text{ GeV}, \quad m(e_{\text{out}}^\pm, \gamma) > 4 \text{ GeV}, \quad (3.4a)$$

$$0.1 \text{ GeV} < p_{T,e_{\text{out}}^\pm} < 1 \text{ GeV}, \quad \Delta R(e_{\text{out}}^-, e_{\text{out}}^+) > 0.4, \quad \Delta R(e_{\text{out}}^\pm, \gamma) > 0.4. \quad (3.4b)$$

This Bhabha scattering background can be further suppressed to the per mille level by vetos based on reconstructed objects in the electromagnetic calorimeters in the very forward region (BeamCal) [58] by a factor of 0.23% [58, 85]. The black-dotted curve in the left panel of Fig. 2 shows the radiative Bhabha scattering contribution to the total background. One can see that it is more than 2 orders of magnitude smaller than the semi-irreducible one and hence is safely negligible. Unless otherwise specified, our discussion focuses on the semi-irreducible background.

For $\sqrt{s} \leq 1$ TeV, the SM background dominates over the possible signal with cut-off scale $\Lambda = 1$ TeV by at least one order. The situation becomes even worse for a massive DM since a nonzero m_χ will further reduce the final-state phase space. To detect such signal or put meaningful limit on the absorption operators, energy cuts are necessary to suppress background and enhance the signal significance.

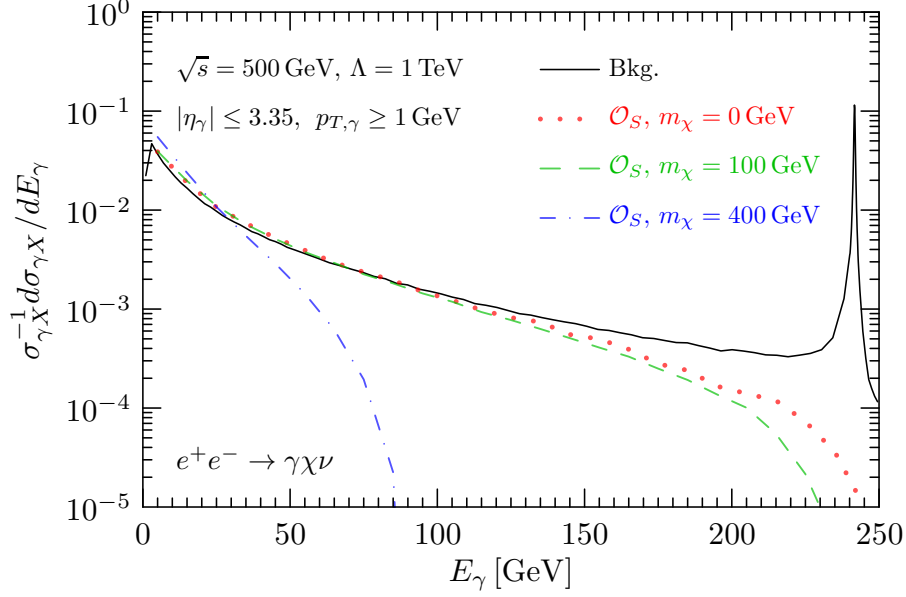


Fig. 3: The normalized photon energy E_γ distribution in the lab frame with $\sqrt{s} = 500$ GeV. For illustration, signals are shown with several dark fermion masses, $m_\chi = 0$ GeV (red-dotted), 100 GeV (green-dashed), and 400 GeV (blue-dash-dotted). The same kinematic cuts $p_{T,\gamma} < 1$ GeV and $|\eta_\gamma| < 3.35$ have been used as before.

3.3. Energy Cut

Since the photon polar angle θ_γ cannot be used to distinguish signals and background, it is desirable to find another observable for the purpose of enhancing the signal-background ratio. With photon being the only detectable particle, one has to resort to the photon property. In addition to θ_γ , the only observable is the photon energy.

Fig. 3 shows the photon energy (E_γ) spectrum at collision energy $\sqrt{s} = 500$ GeV. We can clearly see a peak in the background spectrum (black solid) which is due to the Z resonance in Fig. 1(d). For a two-body phase space of the $Z\gamma$ system, the photon energy is determined by the Z boson mass m_Z and the collision energy \sqrt{s} ,

$$E_\gamma^Z = \frac{1}{2}\sqrt{s} \left(1 - \frac{m_Z^2}{s} \right). \quad (3.5)$$

The peak width is mainly determined by the Z boson width and the ISR. For comparison, the signals (colorful curves) do not have a peak at that place but a continuously decreasing photon spectrum that finally stops at,

$$E_\gamma^\chi \leq \frac{1}{2}\sqrt{s} \left(1 - \frac{m_\chi^2}{s} \right). \quad (3.6)$$

This upper limit is reached when the $\chi\bar{\nu}$ ($\bar{\chi}\nu$) system has the minimal invariant mass, $m_X \geq m_\chi$.

With such difference in the photon energy spectrum, it is possible to cut off a significant part of the background with

$$E_\gamma < \bar{E}_\gamma \equiv \min \{ E_\gamma^Z - 5\Gamma_Z, E_\gamma^\chi \}, \quad (3.7)$$

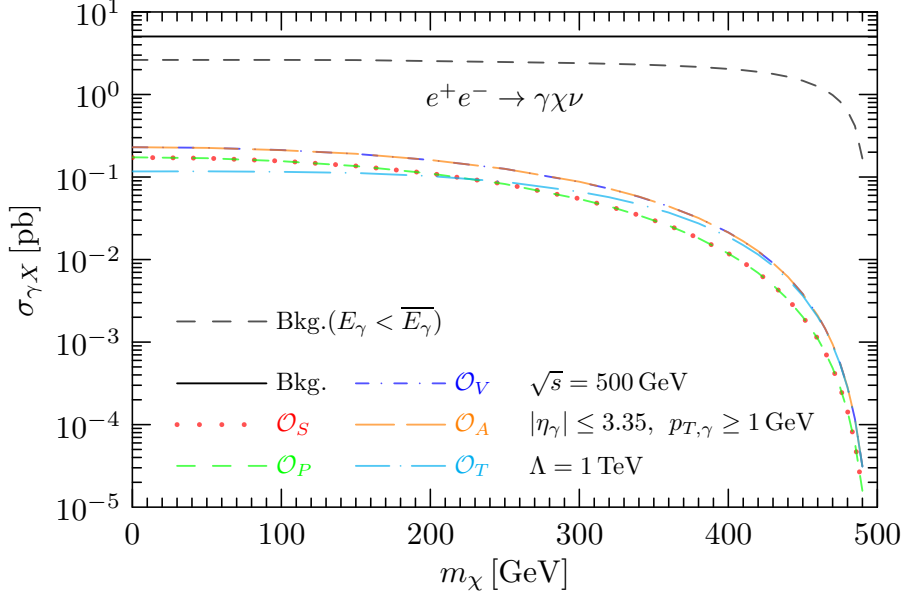


Fig. 4: The mono-photon production cross sections at $\sqrt{s} = 500$ GeV as function of the dark fermion mass m_χ .

to enhance the signal significance. The black-dashed curve in Fig. 4 shows the irreducible background after applying the above kinematic cut. For small m_χ , the background event rate reduces by roughly a factor of 2. Although the Z resonance peak can be removed, the low-energy peak with E_γ approaching 0, which is caused by the W mediated diagrams in Fig. 1(c), almost overlaps with the signal spectrum and hence cannot be effectively suppressed. It is interesting to observe that larger reduction can be achieved for larger dark fermion mass m_χ as shown by the black dashed line in Fig. 4. This is because the photon energy cut \bar{E}_γ is a function of the dark fermion mass m_χ via the E_γ^χ defined in Eq. (3.6).

Fig. 4 shows the m_χ dependence of the total cross sections with the kinematic cuts in Eq. (3.3) and Eq. (3.7). As expected, the signal cross sections decrease with the dark fermion mass m_χ and vanish when approaching the kinematically allowed upper limit, $m_\chi \leq \sqrt{s}$. Even after applying the energy cut, the SM background still dominates over signals with $\Lambda = 1$ TeV. More powerful measures such as the beam polarizations are necessary as we elaborate below.

3.4. Beam Polarization

After suppressing the Z resonance peak by photon energy cut in Eq. (3.7), the major SM background comes from the W mediated diagrams in Fig. 1. Note that the charged current interactions mediated by the SM W only involve left-handed fermions. This allows the possibility of using the beam polarizations for further suppression of background which is one of the most important advantages of e^+e^- colliders.

The cross sections with electron and positron beam polarization rates P_{e^-} and P_{e^+} , respec-

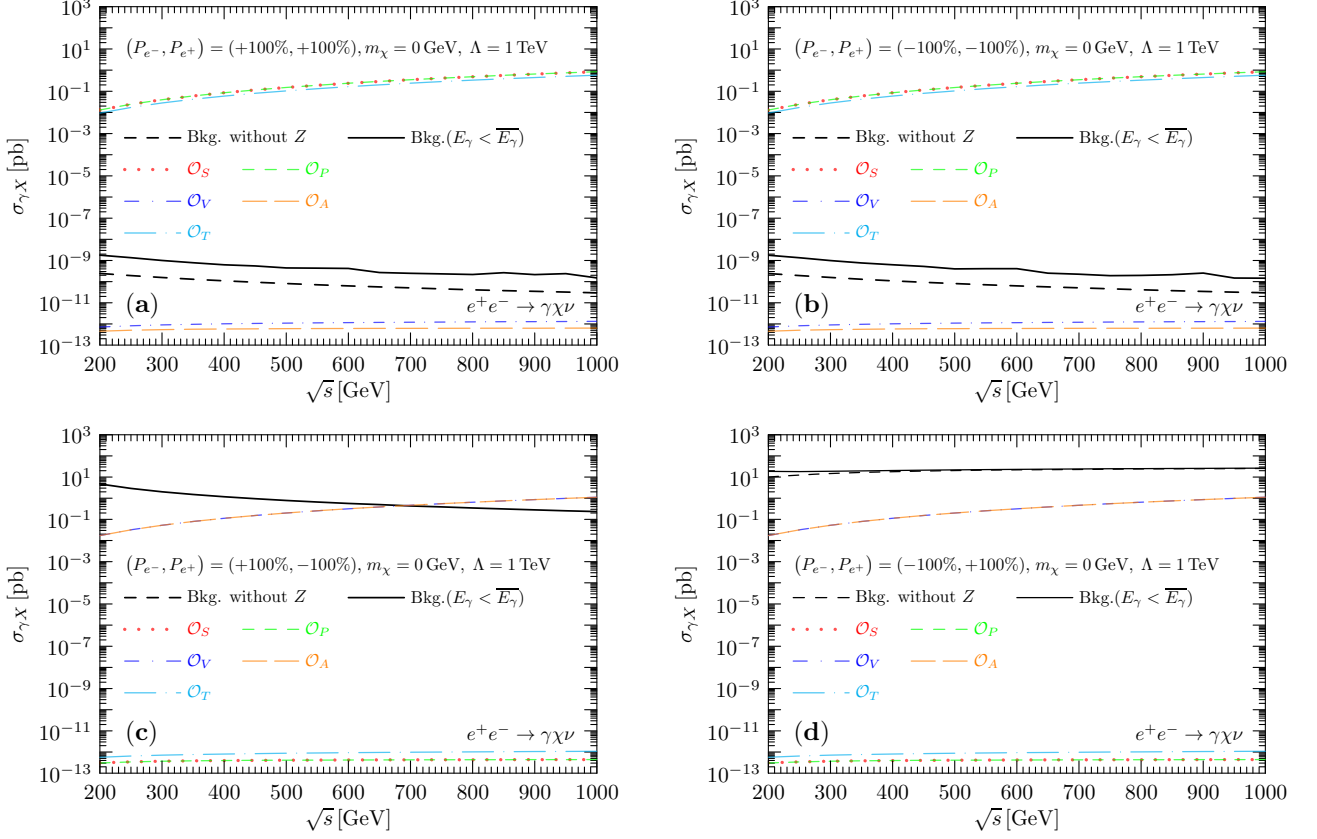


Fig. 5: The mono-photon cross section with purely polarized beams $(P_{e-}, P_{e+}) = (+100\%, +100\%)$ (top-left), $(-100\%, -100\%)$ (top-right), $(+100\%, -100\%)$ (bottom-left), and $(-100\%, +100\%)$ (bottom-right), respectively. The signal ones (colorful non-solid) are shown with vanishing dark fermion mass $m_\chi = 0$ GeV and cut-off scale $\Lambda_i = 1$ TeV. The black curves show the semi-irreducible backgrounds with (black solid) and without (black dashed) the Z resonance contribution. Note that the black-dashed curve with beam polarization $(P_{e-}, P_{e+}) = (+100\%, -100\%)$ is too small ($\sim 10^{-24}$ pb) and lies outside the plot region.

tively, are given (in helicity basis) by,

$$\sigma(P_{e-}, P_{e+}) = \sum_{\lambda_{e-}, \lambda_{e+} = \pm 1} \frac{1 + \lambda_{e-} P_{e-}}{2} \frac{1 + \lambda_{e+} P_{e+}}{2} \sigma_{\lambda_{e-} \lambda_{e+}}, \quad (3.8)$$

where $\sigma_{\lambda_{e-} \lambda_{e+}}$ are the cross sections with purely polarized beams, $\lambda_{e\pm} = \pm 1$, in the helicity basis. The electron and positron polarization rates are defined as $P_{e\pm} \equiv (\phi_{e\uparrow}^\pm - \phi_{e\downarrow}^\pm) / (\phi_{e\uparrow}^\pm + \phi_{e\downarrow}^\pm)$ with $\phi_{e\uparrow, \downarrow}^\pm$ being the positron/electron fluxes with positive (\uparrow) and negative (\downarrow) helicities, respectively. Then the prefactor $(1 + P_{e\pm})/2$ is the weight for each beam polarization component.

Fig. 5 shows the polarization effects on the signal (colorful non-solid lines) and background (black) cross sections. The electron and positron beams have $P_{e\pm} = \pm 100\%$ polarizations. Since only the left-handed electron and positron can participate the SM charged current interactions, either $P_{e-} = +100\%$ or $P_{e+} = -100\%$ suppresses the two Feynman diagrams in the middle of Fig. 1 explaining why the black dashed lines in the first three subplots of Fig. 5 are highly suppressed. To make this effect more transparent, the black dashed lines are obtained with the Z resonance being manually removed and only the W mediated diagrams included. In

particular, Fig. 5(c) even does not contain a black dashed line due to the double suppression of both $P_{e-} = +100\%$ and $P_{e+} = -100\%$. The residual contributions for the two black dashed lines in Fig. 5(a) and Fig. 5(b) exist only because of the chirality flip with a nonzero electron mass. For $\sqrt{s} = 500 \text{ GeV}$, the size of the chirality flip effect is roughly $m_e/\sqrt{s} \sim \mathcal{O}(10^{-6})$ at the amplitude level which is squared to account for the $\mathcal{O}(10^{-12})$ suppression factor at the cross section level. With double suppression for Fig. 5(c), the black dashed line with $\mathcal{O}(10^{-24}) \text{ pb}$ is way out of the plot range. For the polarization combinations $P_{e-} = -100\%$ and $P_{e+} = +100\%$ in Fig. 5(d), the W contribution is almost not affected. To suppress the W mediated contributions, it is better to have either $P_{e-} = +100\%$ or $P_{e+} = -100\%$.

For the Z resonance, the electron and positron polarizations need to be chosen coherently since no single one can suppress its contribution. This is because the Z boson mediated neutral current can couple with both left- and right-handed fermions. However, the vector and axial-vector currents do not flip chirality. With mismatched polarizations, either $P_{e-} = +100\%$ with $P_{e+} = +100\%$ or $P_{e-} = -100\%$ with $P_{e+} = -100\%$, the Z resonance can also be suppressed. These can be seen in the two suppressed black solid lines in the first two panels of Fig. 5.

Combing the requirements for suppressing the W and Z mediated diagrams, it seems only the two combinations in the first two panels of Fig. 5 satisfy our purpose. Unfortunately, the signals will also be affected, especially for the vector and axial-vector type operators in Eq. (2.1). With the same chirality structure as the SM neutral current interactions, the cross section for these two operators will also be significantly suppressed. Non-pure beam polarization also has its reason to stay.

Another reason for impure polarization is the practical possibility. It is very difficult to make a beam 100% polarized. Fig. 6 shows the polarized cross sections with typical beam polarizations $P_{e-} = \pm 80\%$ and $P_{e+} = \pm 30\%$. Again, the black solid (dashed) curves show the result with (without) the Z resonance contribution. For the W only result (black dashed line), the only sizable contribution comes from the polarization configuration of $P_{e-} = -100\%$ and $P_{e+} = +100\%$ in Fig. 5(d). Consequently, the black dashed lines in all the panels of Fig. 6 can be simply rescaled according to the polarization weighting factors in Eq. (3.8). The largest one is $\sigma_{\text{Bkg}}(-80\%, +30\%)$ in Fig. 6(d) which is approximately 58.5% of the maximally polarized one $\sigma_{\text{Bkg}}(-100\%, +100\%)$. The other channels are roughly suppressed by a factor of 3.5% for $\sigma_{\text{Bkg}}(+80\%, -30\%)$ (bottom-left panel), 6.5% for $\sigma_{\text{Bkg}}(+80\%, +30\%)$ (top-left panel), and 31.5% for $\sigma_{\text{Bkg}}(-80\%, -30\%)$ (top-right panel). Although the W mediated contributions are suppressed to be negligibly small in the first three panels of Fig. 5, its effect remains quite sizable for impure polarization configurations. The similar thing also happens for the Z resonance. In all the four panels of Fig. 6, the SM background almost always dominates over signals. Nevertheless, the energy cut and polarization already bring the SM background event rate quite close to the signal ones. With the expected high precision measurement, it is still quite promising to probe the fermionic absorption DM scenario ($m_\chi = 0 \text{ GeV}$) at the future lepton colliders.

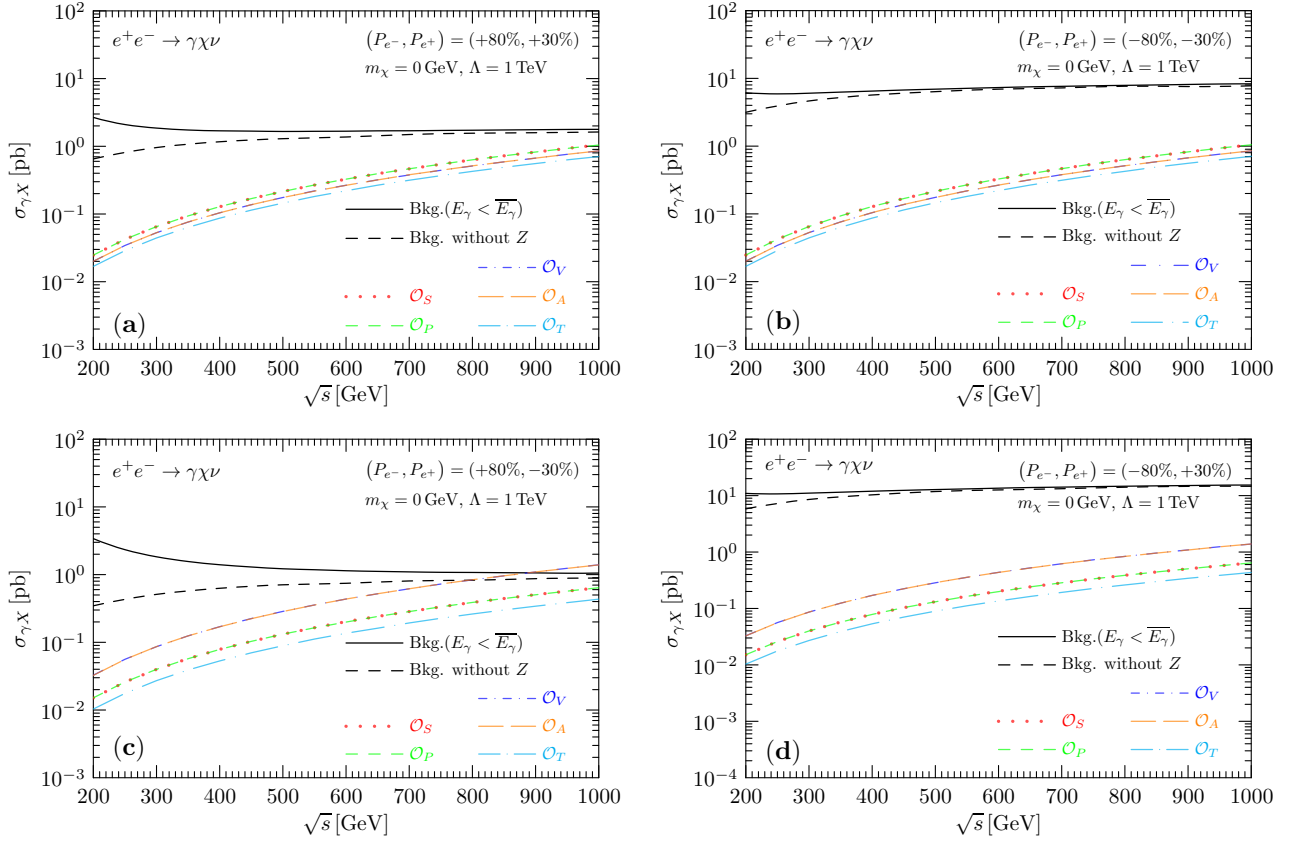


Fig. 6: The mono-photon cross sections with impure beam polarizations $(P_{e^-}, P_{e^+}) = (+80\%, +30\%)$ (top-left), $(-80\%, -30\%)$ (top-right), $(+80\%, -30\%)$ (bottom-left), and $(-80\%, +30\%)$ (bottom-right), respectively.

Impure polarization also has a benefit of allowing a sizable event rate for all types of effective operators. The signals (colorful non-solid curves) in Fig. 6 are shown with vanishing dark fermion mass $m_\chi = 0$ GeV and cut-off scale $\Lambda_i = 1$ TeV. We can see that for the five operators, their cross sections are quite close to each other. The smallest difference between the signal and background cross sections happens for the left two panels with $P_{e^-} = 80\%$ and particularly together with $P_{e^+} = -30\%$ which can be treated as our optimal choice or requirement.

3.5. Projected Sensitivity

There are several proposals for the future e^+e^- colliders, CEPC [86], FCC-ee [87, 88], ILC [89, 90], and CLIC [91]. While circular colliders (CEPC and FCC-ee) can provide higher luminosity, the linear ones (ILC and CLIC) can reach higher energy and are much easier to have polarized beams.

- The CEPC has three different running modes [86], the Higgs factory mode at $\sqrt{s} = 240$ GeV with a total luminosity of 5.6 ab^{-1} , the Z factory mode at $\sqrt{s} = 91.2$ GeV with a total luminosity of 16 ab^{-1} , and the WW threshold scan in the range of $\sqrt{s} \sim 158\text{--}172$ GeV with a total luminosity of 2.6 ab^{-1} . As illustrated earlier, the signal cross sections grow

with \sqrt{s} . So in this paper we consider only the Higgs factory mode that has the highest collision energy at CEPC. Although the beam polarization is difficult at circular colliders, there are already some explorations [92, 93].

- The FCC-ee also runs at the Z pole with a projected luminosity of 150 ab^{-1} and the Higgs mode ($\sqrt{s} = 240 \text{ GeV}$) with a total luminosity of 5 ab^{-1} [87, 88]. The Running mode near the W -pair production threshold, $\sqrt{s} \sim 162.5 \text{ GeV}$, can accumulate a total luminosity of 12 ab^{-1} . Around the top-pair production threshold, there is a multi-point scan at eight collision energies $\sqrt{s} = (340, 341, 341.5, 342, 342.5, 343, 343.5, 344, \text{ and } 345) \text{ GeV}$ each with a luminosity of 25 fb^{-1} . The beam polarization has also been proposed which is under study for the Z -pole and W -pair production modes [94–96]. Although the top-pair production mode has much higher energy, the luminosity is much smaller. So the preferred running mode at FCC-ee is still the Higgs factory one with both high enough energy and large luminosity. Due to similarity with CEPC for the Higgs factory mode, we take CEPC as an example in later discussions and the results can scale accordingly for FCC-ee.
- The ILC was proposed to run at $\sqrt{s} = 500 \text{ GeV}$, and will collect a data set of 4 ab^{-1} in total [89]. Furthermore, the beam polarization will be studied according to the H20 running scenario [90] for optimizing the physics performance. More recently, ILC running at $\sqrt{s} = 250 \text{ GeV}$ with a total luminosity 2 ab^{-1} has also been proposed [97]. Since it is much similar to the Higgs factory mode at CEPC, here we consider only the case of $\sqrt{s} = 500 \text{ GeV}$ which has much higher energy. The ILC also plans to run at $\sqrt{s} = 90 \text{ GeV}$ and 160 GeV with smaller total luminosities of 100 fb^{-1} and 500 fb^{-1} [90], respectively.
- The CLIC is designed to run at 380 GeV , 1.5 TeV , and 3 TeV with total integrated luminosities of 1 ab^{-1} , 2.5 ab^{-1} , and 5 ab^{-1} , respectively [91]. We focus on the highest energy case of 3 TeV with the largest luminosity for demonstration. This does not mean the 1.5 TeV mode is not important. Even though running modes with an 80% polarization has also been proposed, it only applies for the electron beam but not the positron one. So we only consider the unpolarized case at CLIC.

	CEPC	ILC			CLIC
$\sqrt{s} [\text{GeV}]$	240	500			3000
(P_{e-}, P_{e+})	(0%, 0%)	(0%, 0%)	$(\pm 80\%, \mp 30\%)$	$(\pm 80\%, \pm 30\%)$	(0%, 0%)
$\mathcal{L} [\text{ab}^{-1}]$	5.6	4	1.6	0.4	5

Table 1: *The running modes and the corresponding projected luminosities at the future e^+e^- colliders.*

The typical running modes and projected luminosities used in our simulations are listed in Table 1.

As demonstrated earlier, the photon energy E_γ is the only sensitive observable for distinguishing signals and background. In practical measurement, the photon energy is smeared by various factors such as the ISR and detector resolutions [58]. Since both signals and background have continuous E_γ distributions, the spectrum is not significantly modified. But the

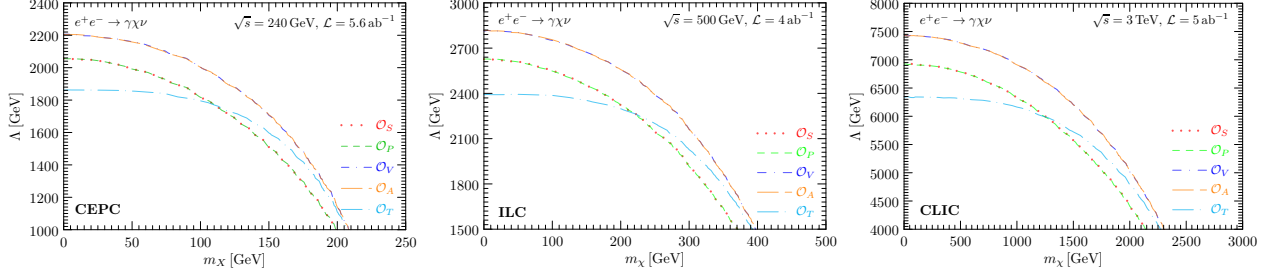


Fig. 7: The 95% exclusion sensitivities for the mono-photon search at CEPC (left), ILC (middle), and CLIC (right).

total cross sections are reduced with relatively stronger dependence on the collision energy \sqrt{s} that is depleted by the ISR. In this paper, the ISR effect is taken into account by using the plugin MGISR [98, 99] to MadGraph5 [81].

The events at these future e^+e^- colliders are first selected with the following minimal cuts,

$$p_{T,\gamma} > 0.5 \text{ GeV}, \quad |\eta_\gamma| < 2.65, \quad \text{CEPC}; \quad (3.9a)$$

$$p_{T,\gamma} > 6 \text{ GeV}, \quad |\eta_\gamma| < 2.79, \quad \text{ILC}; \quad (3.9b)$$

$$p_{T,\gamma} > 60 \text{ GeV}, \quad |\eta_\gamma| < 2.44, \quad \text{CLIC}. \quad (3.9c)$$

For CEPC, the rapidity cut is chosen according to its Conceptual Design Report (CDR) [86] for the Electromagnetic Calorimeter (EMC) coverage and the $p_{T,\gamma}$ cut is slightly larger to reduce the radiative Bhabha background [66]. Due to the BeamCal configuration, two different cuts $p_{T,\gamma} > 1.92 \text{ GeV}$ and $p_{T,\gamma} > 5.65 \text{ GeV}$ are needed at ILC [58, 85]. For simplicity, we use a universal transverse momentum cut $p_{T,\gamma} > 6 \text{ GeV}$ while the rapidity cut is taken from [58]. The cuts for CLIC follow those in [100].

The signal significance is also be affected by the photon reconstruction efficiency. It can reach above 99% for $E_\gamma < 2 \text{ GeV}$ and $7^\circ < \theta_\gamma < 173^\circ$ ($|\eta_\gamma| < 2.79$) at ILC [85] and similarly at CLIC [100]. At CEPC, the identification efficiency is nearly 100% for photons with $E_\gamma > 5 \text{ GeV}$ and more than 99% of their energy can be reconstructed [86]. Hence we simply take 100% reconstruction efficiency for illustration.

Since the photon energy E_γ spectrum for signals and background are quite similar in the signal dominating region with small E_γ (see Fig. 3), the signal significance can not be enhanced much by data binning. So we simply use the total event number to estimate the experimental sensitivity with the following χ^2 ,

$$\chi^2 = \frac{(N^{\text{Sig}})^2}{N^{\text{Bkg}} + N^{\text{Sig}}}, \quad (3.10)$$

with N^{Bkg} and N^{Sig} being the background and signal event numbers, respectively.

Fig. 7 shows the expected 95% exclusion limits at CEPC (left), ILC (middle), and CLIC (right) with unpolarized beams. As we have shown in Fig. 3, total cross sections of the scalar

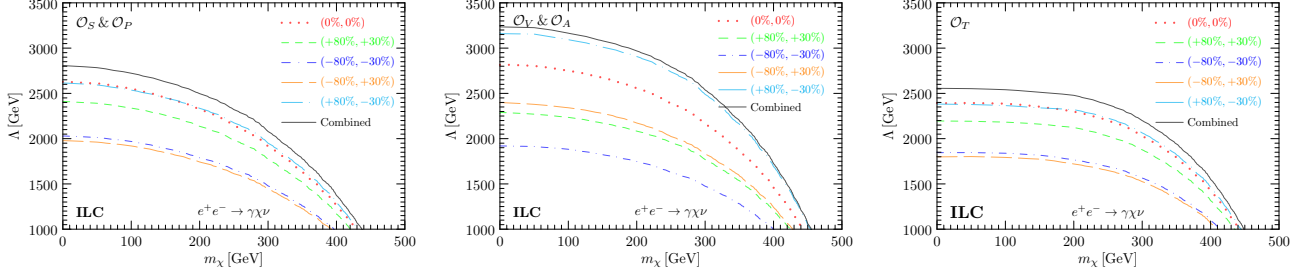


Fig. 8: The expected 95% exclusion limits provided by the mono-photon channel at ILC with beam polarizations $(P_{e-}, P_{e+}) = (\pm 80\%, \pm 30\%)$ and the corresponding projected luminosities listed in Table. 1. Three cases of (pseudo-)scalar (left), (axial-)vector (middle), and tensor (right) operators are shown. A combined exclusion limit from all the four polarization configurations are also shown by black-solid line. For comparison, the red-dotted lines are for unpolarized beams while the black solid lines for combined polarization configurations.

(vector) and pseudo-scalar (axial-vector) are the same, and hence the mono-photon process is unable to distinguish the corresponding Lorentz structures of the effective operators. We can also see this property in Fig. 7, where the exclusion curves for scalar (vector) and pseudo-scalar (axial-vector) completely overlap. With the vector and axial-vector operators having the largest cross sections for a universal cut-off scale Λ , the expected exclusion limits are the strongest ones. For a massless dark fermion ($m_\chi = 0$), the exclusion limits reach 2.2 TeV, 2.8 TeV and 7.4 TeV at $\sqrt{s} = 240$ GeV, 500 GeV, and 3 TeV, respectively. For comparison, the exclusion limits for the scalar and pseudo-scalar operators are slightly lower, reaching 2.0 TeV, 2.6 TeV and 6.9 TeV, respectively. The tensor operator has the weakest limits at 1.8 TeV, 2.4 TeV, and 6.3 TeV, respectively. Due to the phase space suppression, the exclusion limits reduce with increasing dark fermion mass. With higher beam energy, the exclusion limits increase quite significantly.

The effect of beam polarizations are studied at $\sqrt{s} = 500$ GeV with typical beam polarizations $P_{e-} = \pm 80\%$ and $P_{e+} = \pm 30\%$ at ILC for illustration. Using the luminosities listed in Table 1, Fig. 8 shows the expected 95% exclusion limits for the (pseudo-)scalar (left), (axial-)vector (middle), and tensor (right) operators. For comparison, the exclusion limits with unpolarized beams are also shown by red-dotted lines. Of the four different beam polarization configurations, $(P_{e-}, P_{e+}) = (+80\%, -30\%)$ is the most sensitive one as expected. This is particularly useful for the (axial-)vector operator. In addition, the combined exclusion limit (black-solid) from all the four polarization configurations provides further enhancement.

4. Electron-Positron Pair Production Associated with Missing Energy

In addition to photon, the charged electron/positron that appears in the absorption operators is also detectable at the future e^+e^- colliders. For example, the electron-positron pair production associated with missing energy $e^+e^- \rightarrow e^+e^- + \cancel{E}_T$ can also probe the $\chi\nu e^+e^-$ coupling. Since

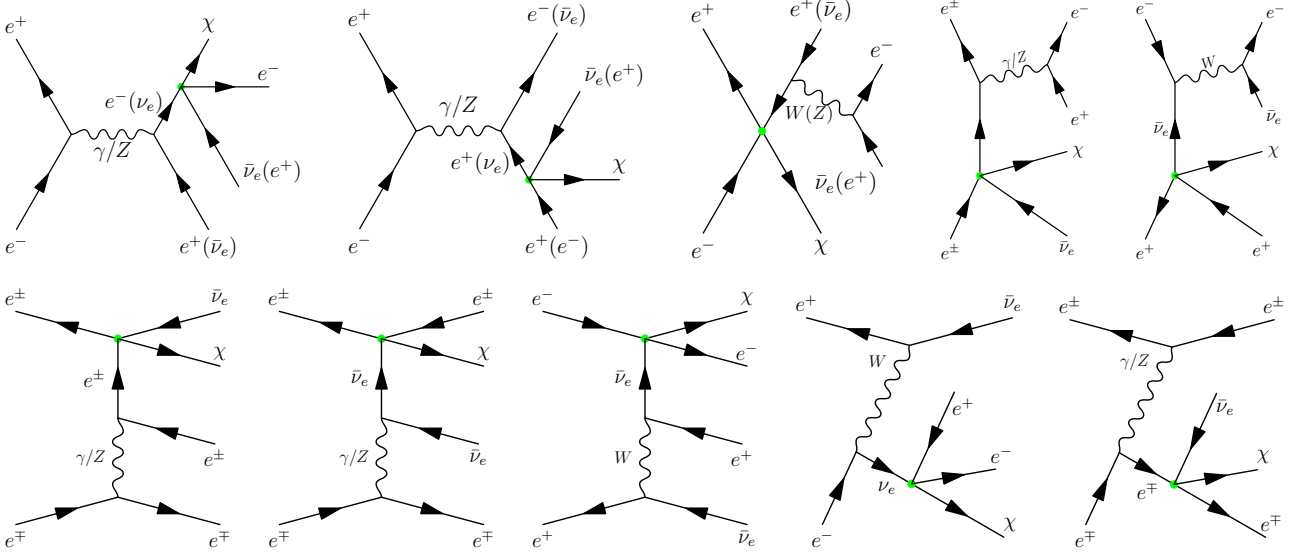


Fig. 9: The signal Feynman diagrams for the electron-positron pair production associated with missing energy, $e^+e^- \rightarrow e^+e^- \cancel{E}_T$.

both the dark fermion χ and neutrino are invisible, two channels can contribute,

$$e^+ + e^- \rightarrow e^+ + e^- + \nu_e + \bar{\chi} (\chi + \bar{\nu}_e), \quad (4.1a)$$

$$e^+ + e^- \rightarrow e^+ + e^- + \nu_e + \bar{\nu}_e, \quad (4.1b)$$

whose Feynman diagrams are shown in Fig. 9 and Fig. 10, respectively.

For the first channel in Fig. 9, each diagram contains a single effective operator labeled by the green dot. So the amplitude contains a factor $1/\Lambda^2$ and the cross section has $1/\Lambda^4$. The Feynman diagrams in the first row each contains an s -channel resonance at either the neutral γ/Z or the charged W pole. For comparison, those in the second row arise from the t -channel processes. All these diagrams have the dark fermion χ or $\bar{\chi}$ in the final state, although only χ is shown in Fig. 9 for simplicity.

However, missing energy does not mean that χ has to appear as a final-state particle. Instead,

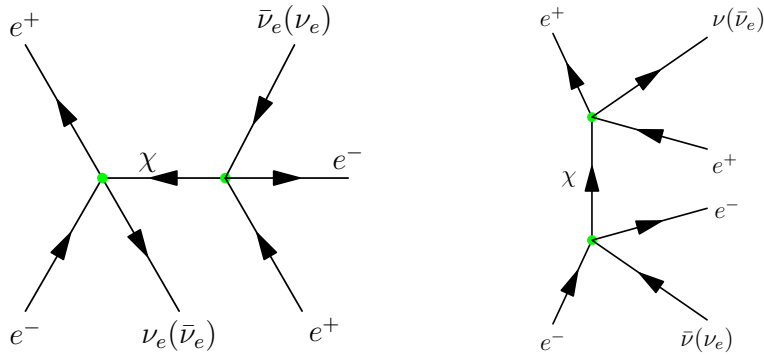


Fig. 10: The signal Feynman diagrams for the electron-pair production with missing energy carried away by a neutrino pair, $e^+e^- \rightarrow e^+e^- \nu \bar{\nu}$, that can interfere with the SM backgrounds.

it can appear as an intermediate particle with neutrino playing its role to serve as missing energy. To achieve that, two effective operators are necessary to provide two χ lines to form a propagator as shown in Fig. 10. Such diagram already receives a factor of $1/\Lambda^4$ suppression at the amplitude level. To be comparable with the single-operator processes in Fig. 9, an interference with a SM process that is not suppressed by Λ is required. In total, 56 Feynman diagrams can contribute to such SM process with $e^+e^-\nu_e\bar{\nu}_e$ final states whose Feynman diagrams are omitted for simplicity but can be easily generated with various tools on market such as CompHEP [101], CalcHEP [102], and MadGraph5 [81]. However, since the SM processes are dominated by nearly on-shell intermediate vector bosons (Z and W^\pm), the interference effects are significantly reduced with limited phase space. The SM background is shown as black lines in Fig. 11. Note that the two sudden increases around $\sqrt{s} \approx (100 \sim 200)$ GeV come from the W and Z pair production thresholds.

The left panel of Fig. 11 shows the interference contributions (colofull non-solid curves) in comparison with the corresponding pure SM background (black-solid). Note that the sign of the interference contribution depends on the collision energy \sqrt{s} and the Lorentz structure of the effective four-fermion operators. For simplicity, only the magnitudes of the interference contributions are shown without their signs. One can clearly see that even though the signal cross sections (with $\Lambda = 1$ TeV and $m_\chi = 0$ GeV) grow with \sqrt{s} , it is still more than 3 orders of magnitude smaller than the background at $\sqrt{s} = 1$ TeV.

For comparison, the cross sections of the purely new physics channels in Fig. 9 grow rapidly with \sqrt{s} , as shown in the right panel of Fig. 11. At $\sqrt{s} = 1$ TeV, their cross sections with $m_\chi = 0$ GeV and $\Lambda = 1$ TeV are about just 1 order of magnitude smaller than and quickly exceed the SM background for $\sqrt{s} \gtrsim 1$ TeV. It is of great advantages for searching the electron-positron pair production associated with missing energy at CLIC that has running modes at 1.5 TeV and 3 TeV. Then, the interference channels in Fig. 10 can be safely ignored.

Since things are not settled yet to foresee which future e^+e^- collider would finally get running, we also study the projected sensitivities at CEPC and ILC. Before doing specific analysis, the e^+e^- events are selected by some basic cuts,

$$|\eta_{e^\pm}| < 2.5, \quad p_{T,e^\pm} > 5 \text{ GeV}, \quad (4.2)$$

which can universally apply for CEPC, FCC-ee, ILC, and CLIC. Below we will show more details about this process.

4.1. Differential Cross Sections for Distinguishing Signals and Background

Fig. 12 shows some differential distributions of the $e^+e^- \rightarrow e^+e^-E_T$ process at CLIC with $\sqrt{s} = 3$ TeV and selected by kinematic cuts in Eq. (4.2). Both signals and background have a Z resonance peak in the invariant mass $m_{e^+e^-}$ spectrum, which are shown as Fig. 12(a). While

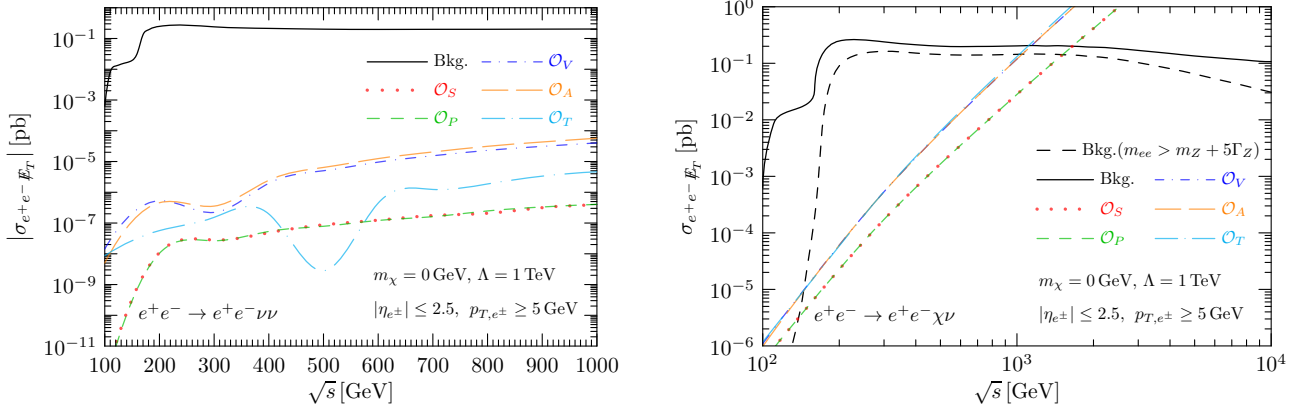


Fig. 11: **Left panel:** The $e^+ + e^- \rightarrow e^+ + e^- + \nu + \bar{\nu}$ cross sections given by purely the SM contribution (black-solid) as well as the interference (colorful non-solid) between the SM contribution and the effective four-fermion operators. **Right panel:** The cross sections of the $e^+e^- + \nu + \bar{\chi}$ and $\chi + \bar{\nu}$ signal process and the purely SM background $e^+e^- \rightarrow e^+e^- + 2\nu$.

the signal has a bump in the range of $500 \text{ GeV} \lesssim m_{e^+e^-} \lesssim 2000 \text{ GeV}$, the SM background curve is more flat. In other words, the middle region of the $m_{e^+e^-}$ -distribution provides more signal significance than the region around the Z resonance.

However, the Z resonance in the signal and background events are quite different. For background, the Z bosons are pairly produced via t -channel ISR process and then decay into electron-positron and neutrino pairs, $e^+e^- \rightarrow Z + Z \rightarrow 2e + 2\nu$. Such on-shell Z bosons move in the forward and backward regions, as can be seen in Fig. 12(c). In addition, the transverse momentum p_{T,e^+e^-} of the e^+e^- system tends to have small values as shown in Fig. 12(b). In contrast, the signal Z resonance is not that forwarded/backwarded and hence the electron-positron pair can have larger transverse momentum. These features can be used to distinguish signals from the SM background.

Among various operators, the differential distributions are not that different. The kinematic distributions of the e^+e^- system as a whole cannot help much to distinguish different signals. This is because the electron bilinear in the effective operators Eq. (2.1) behaves like an effective particle. For example, $\bar{e}e$ ($\bar{e}\gamma_5 e$) and $\bar{e}\gamma_\mu e$ ($\bar{e}\gamma_\mu\gamma_5 e$) for the e^+e^- system can be treated as a scalar and vector particle, respectively. The kinematic observable such as $m_{e^+e^-}$, p_{T,e^+e^-} , or $\cos\theta_{e^+e^-}$ apply for both scalar and vector particles. Without reconstructing the total spin of the e^+e^- system, there is no way to distinguish different operators. The same logic also works for the tensor operator.

Fortunately, the situation can be improved by using the distributions of the individual final-state electron or positron that are shown in the second and third rows of Fig. 12. Comparing the situations at CLIC (middle row) and ILC (bottom row), the difference among signals is larger with smaller collision energy. CLIC has large enough difference in only the $\cos\theta_{e^-}$ -distribution. In contrast, the E_{e^-} and p_{T,e^-} distributions are also quite different at ILC. It is of

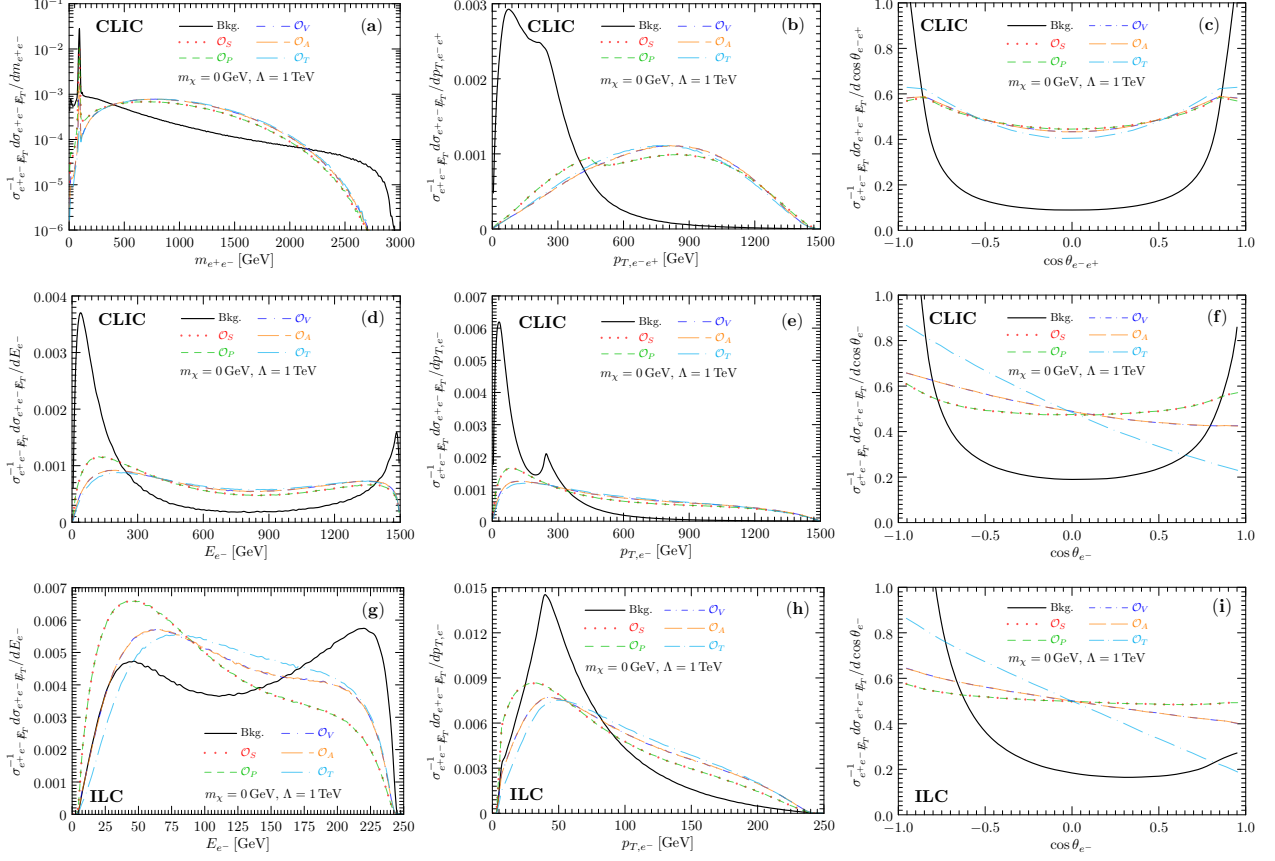


Fig. 12: The differential cross sections of the $e^+e^- \rightarrow e^+e^- + \cancel{E}_T$ channel. For signals (colorful non-solid curves), only $e^+e^- + \nu + \bar{\chi} (\chi + \bar{\nu})$ are taken into account while the black-solid curves show the SM background $e^+e^- \rightarrow e^+e^- + 2\nu$.

great advantages for the $e^+e^- \cancel{E}_T$ search at future lepton colliders to overcome the shortcoming of the mono-photon channel.

For the electron p_T distributions, the background has much narrower peak than signals. This is because both the background e^+e^- and $\nu\bar{\nu}$ systems arise from the Z resonance. Consequently, the electron pair invariant mass $m_{e^+e^-}^2 = m_Z^2$ is fixed by the Z boson mass. In the rest frame of Z , electron carries energy $m_Z/2$ and its angular spectrum follows $d \cos \theta$ with even distribution for $\cos \theta$. Since $p_T \propto \sin \theta$, its probability distribution scales as $\tan \theta$ which diverges at $\theta \rightarrow 90^\circ$. In other words, the electron transverse momentum peaks at $m_Z/2$ in the Z rest frame. Since the ISR Z bosons move in the forward and backward regions, the electron transverse momentum has roughly the same distribution in the lab frame. That explains why the black curve in Fig. 12(h) has a peak around $m_Z/2$. The same logic applies for the neutrino pair system, $m_{\nu\bar{\nu}}^2 = m_Z^2$, which carries an energy of at least m_Z . For comparison, the signal $\chi\nu$ system can have larger energy to allow the colorful lines in Fig. 12(h) to have more events at the higher end of the p_{T,e^-} distribution.

With more spectrum features than the mono-photon search, especially the apparent difference between signals and background, it makes much more sense to employ binned χ^2 analysis.

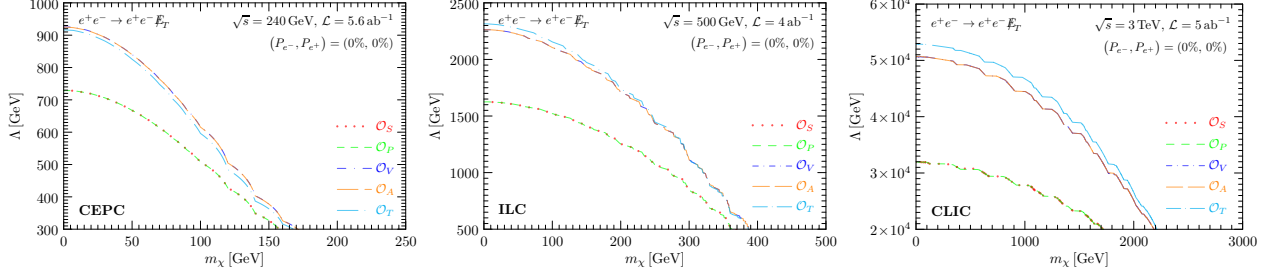


Fig. 13: The expected 95% exclusion limits by the $e^+e^- \rightarrow e^+e^- + \cancel{E}_T$ channel at CEPC (left), ILC (middle), and CLIC (right).

We choose the invariant mass of the electron pair ($m_{e^+e^-}$), the electron energy (E_{e^-}) and transverse momentum (p_{T,e^-}) as three representative observables. The experimental significance is estimated by the following χ^2 ,

$$\chi^2 = \sum_a \sum_i \frac{(N_i^{\text{Sig}}(\mathcal{O}_a))^2}{N_i^{\text{Bkg}}(\mathcal{O}_a) + N_i^{\text{Sig}}(\mathcal{O}_a)}. \quad (4.3)$$

Here $\mathcal{O}_a = m_{e^+e^-}$, E_{e^-} , and p_{T,e^-} are the representative observables while $N_i^{\text{Bkg}}(\mathcal{O}_a)$ and $N_i^{\text{Sig}}(\mathcal{O}_a)$ are the background and signal event numbers in the i -th bin of the observable \mathcal{O}_a .

Three typical future e^+e^- colliders (CEPC, ILC, and CLIC) are considered. For CEPC, the detector can identify the prompt leptons with high efficiency and purity [86]. For lepton with energies above 5 GeV, the identification efficiency can be higher than 99% and the misidentification rate smaller than 2%. Similar thing happens at ILC for the tracking efficiency that can reach $\sim 100\%$ for a charged particle with momentum $p > 1$ GeV [89]. Therefore, it is safe to assume 100% efficiency for the electron and positron reconstructions in the following analysis.

Fig. 13 shows the expected 95% exclusion limits at CEPC (left), ILC (middle), and CLIC (right) with unpolarized beams. For all three colliders, the (axial-)vector and tensor operators have the strongest exclusion limits while the (pseudo-)scalar ones are weaker. As expected, the limits increase with the collision energy. With the limits at CEPC being below 1 TeV, ILC can reach about 2.2 TeV, 1.6 TeV, and 2.3 TeV for the (axial-)vector, (pseudo-)scalar, and tensor operators, respectively. The limits further enhance to about 51 TeV, 32 TeV, and 53 TeV at CLIC. Comparing with the mono-photon search in Sec. 3, the $e^+e^- \cancel{E}_T$ channel has lower sensitivity at CEPC but can double the values at CLIC due to the fast increase of cross section with the collision energy \sqrt{s} .

4.2. Beam Polarizations for Further Suppressing Background

As discussed in Sec. 3.4, the beam polarization can be used to enhance the signal significance using the parity violation nature of the SM electroweak interactions and the effective operators in Eq. (2.1). Fig. 14 shows the signal and background cross sections as function of the collision

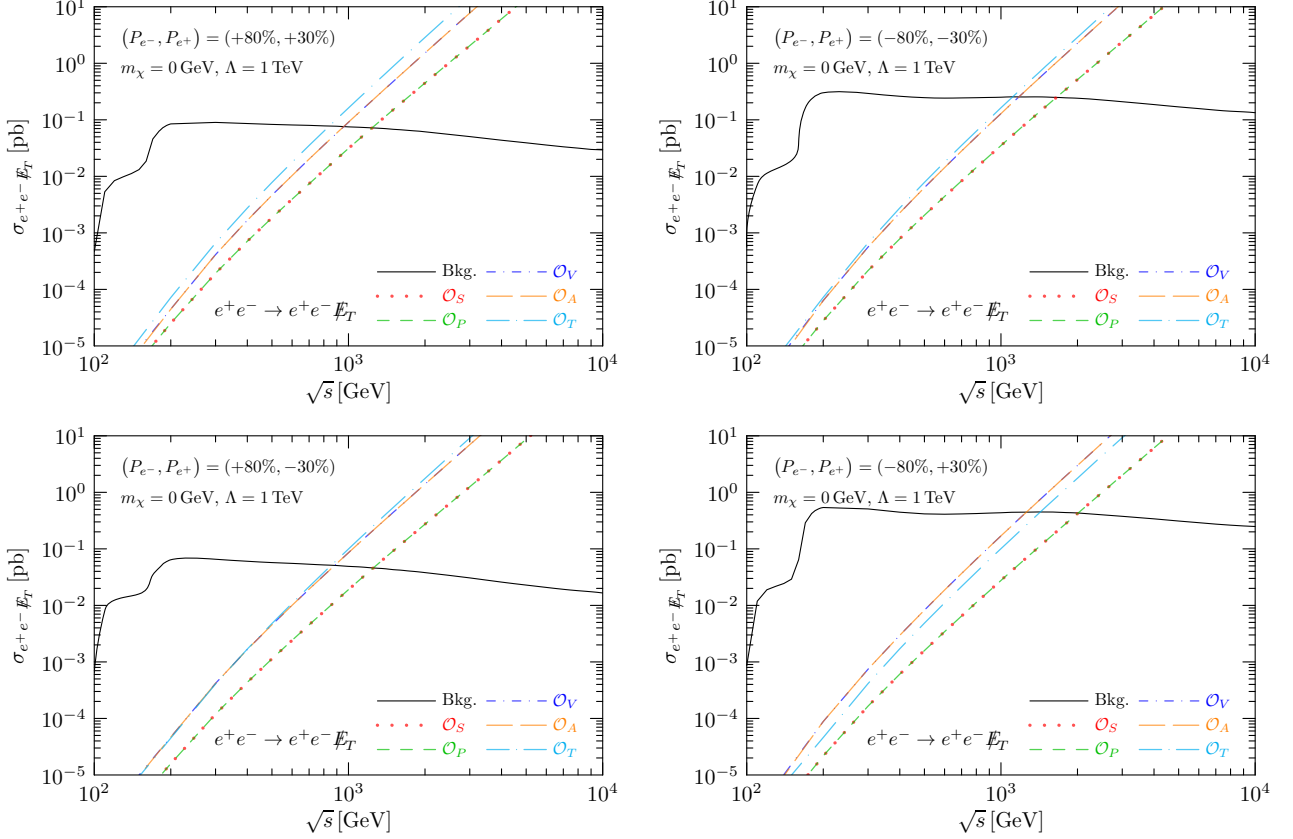


Fig. 14: The polarized cross sections of the $e^+e^- \rightarrow e^+e^- + \cancel{E}_T$ process as function of the collision energy \sqrt{s} . The polarization effects are illustrated with the beam polarization configurations $(P_{e^-}, P_{e^+}) = (+80\%, +30\%)$ (top-left panel), $(-80\%, -30\%)$ (top-right panel), $(+80\%, -30\%)$ (bottom-left panel), and $(-80\%, +30\%)$ (bottom-right panel), respectively. While the signals (colorful non-solid curves) are shown with parameters $m_\chi = 0$ GeV and $\Lambda_i = 1$ TeV, the black-solid curve shows the background from the pure SM contribution to the process $e^+e^- \rightarrow e^+e^- + 2\nu$. All the plots are generated using events passing the kinematic cuts $|\eta_{e^\pm}| < 2.5$ and $p_{T,e^\pm} > 5$ GeV.

energy \sqrt{s} for beam polarizations $P_{e^-} = \pm 80\%$ and $P_{e^+} = \pm 30\%$. Those backgrounds contributed by the SM left-handed charged current can be suppressed by right-handed electron beam as we can see in the top- and bottom-left panels of Fig. 14. Since the SM neutral current has roughly the same coupling strength with the left- and right-handed charged leptons, different beam polarizations make no big difference. Although signals are also reduced, their decrease is much smaller than background to achieve better experimental sensitivity. It turns out the polarization configuration $P_{e^-} = +80\%$ and $P_{e^+} = -30\%$ gives the lowest background. The optimal polarization choice here is the same as the one for the mono-photon search since both have backgrounds due to the same SM weak interactions.

We illustrate the beam polarization effects for ILC at $\sqrt{s} = 500$ GeV with the typical polarization configurations $P_{e^-} = \pm 80\%$ and $P_{e^+} = \pm 30\%$. The expected exclusion limits at 95% C.L. are shown in Fig. 15 for (pseudo-)scalar (left), (axial-)vector (middle), and tensor (right) operators. With a same luminosity for each polarization configuration, $(P_{e^-}, P_{e^+}) =$

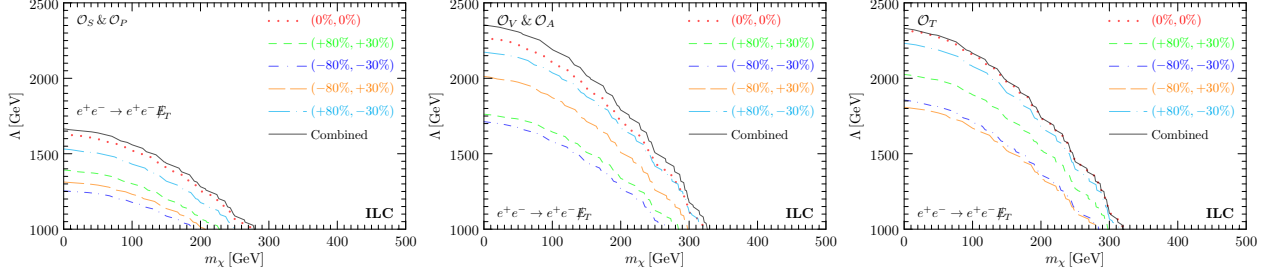


Fig. 15: The expected exclusion limits at 95% C.L. by searching for the $e^+e^- \rightarrow e^+e^- + \cancel{E}_T$ process at ILC ($\sqrt{s} = 500$ GeV) with beam polarizations $(P_{e^-}, P_{e^+}) = (\pm 80\%, \pm 30\%)$ and the corresponding projected luminosities listed in Table 1. The left, middle and right panels show the results for the (pseudo-)scalar, (axial-)vector and tensor operators, respectively. A combined exclusion limit from all the four polarization configurations is also shown by the black-solid line. For comparison, the exclusion limits with unpolarized beams are also shown by red-dotted lines.

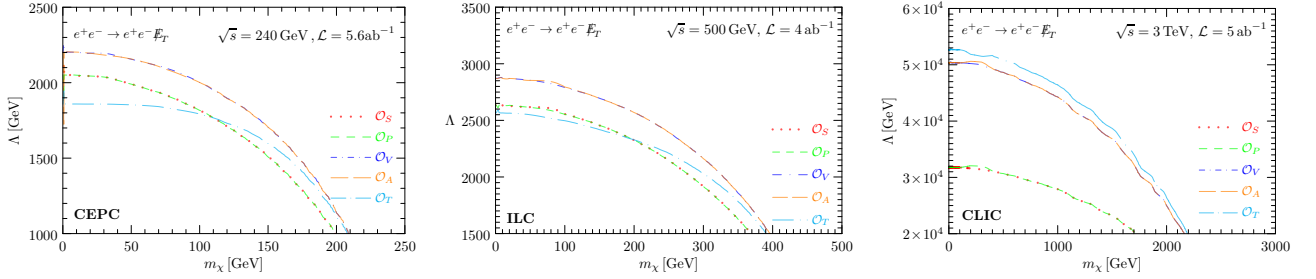


Fig. 16: The combined exclusion limits at 95% C.L. with both the mono-photon and the $e^+e^- \rightarrow e^+e^- + \cancel{E}_T$ searches at CEPC (left), ILC (middle), and CLIC (right). For each detector, we have implemented their projected luminosities as summarized in Table 1. As a conservative estimation, no beam polarization is considered.

(+80%, -30%) has the strongest constraint as expected. For comparison, the exclusion limits with unpolarized beams are also shown as red-dotted lines. With smaller luminosity (1.6 ab^{-1} or 0.4 ab^{-1} as summarized in Table 1), the exclusion limit for individual configuration is weaker than the unpolarized one with 4 ab^{-1} luminosity. But the combined result with all four configurations is indeed stronger.

4.3. Combined Results

Fig. 16 shows the combined sensitivities at the future e^+e^- colliders as previously shown in Fig. 7 and Fig. 13. Since beam polarizations are considered only for ILC, the sensitivity combination is illustrated with unpolarized configurations in Table 1 for equal comparison. With relatively smaller sensitivity enhancement from the $e^+e^- \cancel{E}_T$ search at the low-energy CEPC and ILC, the combined results there are dominated by the mono-photon search in Fig. 7. For CLIC, the improvement of adding the $e^+e^- \cancel{E}_T$ search is quite significant by increasing the limit from around $(6 \sim 7) \text{ TeV}$ to $(30 \sim 50) \text{ TeV}$. The mono-photon search prevails at CEPC and ILC while $e^+e^- \cancel{E}_T$ dominates at CLIC. And $e^+e^- \cancel{E}_T$ at ILC with beam polarizations can help to disentangle various signal operators.

5. Non-Collider Constraints for the Fermionic Absorption DM

As mentioned earlier, the collider search covers the absorption operators with generic dark fermions including the genuine fermionic absorption DM in the sub-MeV mass range. Nevertheless, a DM candidate needs to satisfy more constraints. Since the effective operators in Eq. (2.1) involve neutrinos and the charged electron, various constraints can arise from the DM relic density determined in the early Universe, the astrophysical X -ray and γ ray (X/γ -ray) observations nowadays, and the direct detection experiments on our Earth. Although these constraints have been systematically surveyed in [75], some updates are necessary. With these non-collider constraints being already quite strong, the DM search at the future lepton colliders has its own advantage of significantly improving the sensitivities even for very light DM as summarized in Fig. 17. To make easy comparison with the existing constraints, the collider sensitivities are also shown in terms of $\sigma_{\chi e} v_\chi$,

$$\sigma_{\chi e} v_\chi \approx \frac{1}{\Lambda^4} \frac{m_\chi^2 (2m_e + m_\chi)^2 (2m_e^2 + 4m_e m_\chi + 3m_\chi^2)}{32\pi (m_e + m_\chi)^4}, \quad (5.1)$$

which is a function of m_χ and Λ_i but independent of the DM velocity v_χ [75].

5.1. DM Overproduction in the Early Universe

With highly suppressed coupling strength from cosmology, astrophysics, and direct detection, the fermionic DM needs to be produced through the freeze-in mechanism at temperature around 1 MeV [75]. The production happens via the s -channel e^+e^- pair annihilation $e^-e^+ \rightarrow \nu\bar{\chi}/\bar{\nu}\chi$ or the t -channel scatterings $e^\pm\nu \rightarrow e^\pm\chi$ and $e^\pm\bar{\nu} \rightarrow e^\pm\bar{\chi}$. Although the inverse processes can also happen to reduce the DM amount, its contribution is suppressed by the DM phase space distribution function f_χ which is still in the progress of being built. For completeness, both contributions are included in the Boltzmann equation that governs the DM number density n_χ evolution,

$$\begin{aligned} \frac{dn_\chi}{dt} + 3Hn_\chi = & \int d\Pi_\chi d\Pi_\nu d\Pi_{e^-} d\Pi_{e^+} (2\pi)^4 \delta(p_{e^+} + p_{e^-} - p_\chi - p_\nu) \\ & \times [|\mathcal{M}|_{e^-e^+ \rightarrow \nu\chi}^2 f_{e^+} f_{e^-} (1 - f_\nu)(1 - f_\chi) - |\mathcal{M}|_{\nu\chi \rightarrow e^-e^+}^2 f_\nu f_\chi (1 - f_{e^+})(1 - f_{e^-})] \\ & + 2 \int d\Pi_{e^-} d\Pi_\nu d\Pi'_{e^-} d\Pi_\chi (2\pi)^4 \delta(p_{e^-} + p_\nu - p'_{e^-} - p_\chi) \\ & \times [|\mathcal{M}|_{e^-\nu \rightarrow e^-\chi}^2 f_{e^-} f_\nu (1 - f'_{e^-})(1 - f_\chi) - |\mathcal{M}|_{e^-\chi \rightarrow e^-\nu}^2 f'_{e^-} f_\chi (1 - f_{e^-})(1 - f_\nu)]. \end{aligned} \quad (5.2)$$

The first integration comes from the electron-positron annihilation while the second one from the $e^\pm\nu$ scattering. For simplicity, we first focus on the DM particle χ while its anti-particle has the same evolution behavior and hence the same number density, $n_\chi = n_{\bar{\chi}}$. With χ appearing in the final state of the forward scattering and the initial state of the backward scattering, only ν needs to be taken into consideration. Note that the phase space integration $d\Pi_i \equiv d^3p_i/2E_i(2\pi)^3$

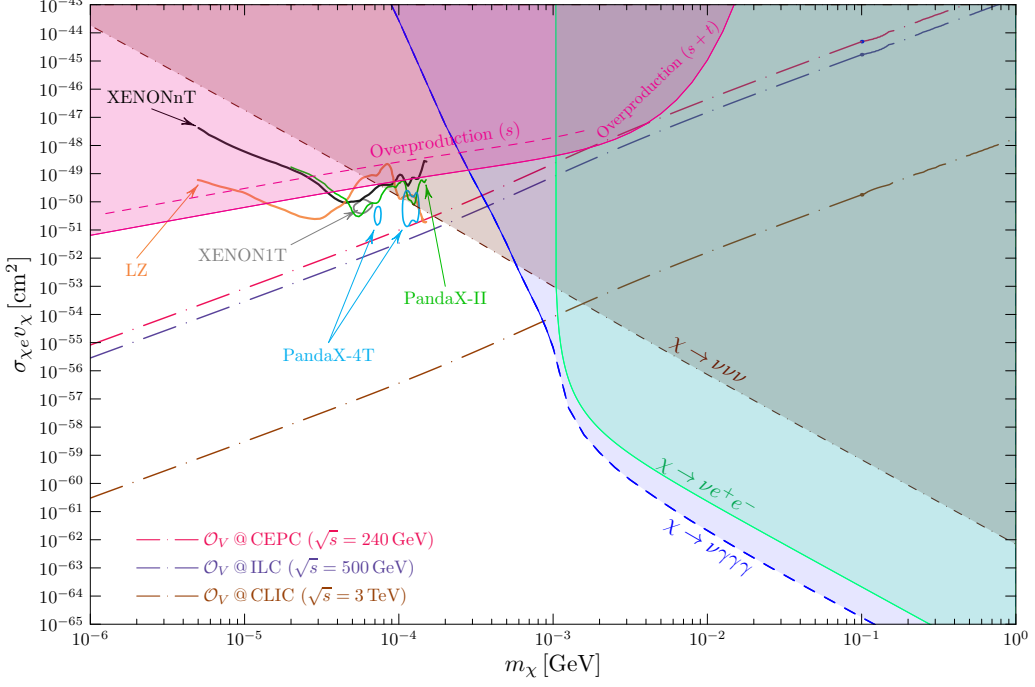


Fig. 17: The updated constraints on the fermionic absorption DM from direct detection experiments (PandaX-II, PandaX-4T, XENONnT, and LZ), cosmology, and astrophysics. For comparison, the projected sensitivities at the future lepton colliders (CEPC, ILC, and CLIC) are shown as long dot-dashed lines.

applies for not just the final-state particles but also their initial counterparts. Inside the square brackets, the first term accounts for the forward reaction while the second one for its inverse. We can see the suppression by the DM phase space distribution f_{χ} appears only in the second terms for the reversed backward reactions. Since both electron and positron can contribute to the t -channel scatterings, a factor of 2 has been assigned to account for their identical contributions.

The above Boltzmann equation can be solved in terms of the DM yield $Y \equiv n_{\chi}/s(T)$ as ratio of the DM number density n_{χ} and the entropy density $s(T)$. We follow the procedures in [75]: 1) neglecting the Pauli blocking effect $1 - f_i \approx 1$ and the reversed reaction contributions that are suppressed by the DM phase space distribution f_{χ} ; 2) approximating the phase space distributions of other particles (electron, positron, and neutrino) by their thermal equilibrium Maxwell-Boltzmann distributions $f_{\text{MB}} = e^{-E/T}$; 3) replacing the scattering amplitudes in Eq. (5.3) by the corresponding cross sections. The final DM yield takes the following compact form,

$$Y(T) = \frac{45M_{\text{P}}}{16\pi^6} \int_T^{T_{\text{max}}} \frac{d\tilde{T}}{1.66\sqrt{g_*(\tilde{T})}\tilde{g}_{*s}(\tilde{T})\tilde{T}^5} \times \left[\int_{s_a}^{\infty} ds (s - 4m_e^2) \sqrt{s} K_1 \left(\frac{\sqrt{s}}{\tilde{T}} \right) \sigma_{e^-e^+} + \int_{s_b}^{\infty} ds \frac{(s - m_e^2)^2}{\sqrt{s}} K_1 \left(\frac{\sqrt{s}}{\tilde{T}} \right) \sigma_{e\nu} \right], \quad (5.3)$$

where $s_a \equiv \max(4m_e^2, m_{\chi}^2)$ and $s_b \equiv (m_e + m_{\chi})^2$. The maximal temperature $T_{\text{max}} = 1$ MeV is the starting point of the DM production. In addition, $g_*(T)$ and $g_{*s}(T)$ are the relativistic degrees

of freedom associated with the energy and entropy densities in the early Universe, respectively. Note that $\tilde{g}_{*s} \equiv g_{*s}/[1 + (T/3g_{*s})(dg_{*s}/dT)]$ to account for the temperature evolution. The Planck mass M_P can trace back to the Newton constant and K_1 is the first modified Bessel function of the second kind. While the pair annihilation cross sections $\sigma_{e^-e^+}$ can be found in [75], the t -channel scattering ones $\sigma_{e\nu}$ are,

$$\sigma_{e\nu}^S = \frac{t_- \left[t_+^2 - 2(4m_e^2 + m_\chi^2)t_+ + 16m_e^2m_\chi^2 + \frac{t_-^2}{3} \right]}{64\pi(s - m_e^2)^2} \frac{1}{\Lambda^4}, \quad (5.4a)$$

$$\sigma_{e\nu}^P = \frac{t_- \left(t_+^2 - 2m_\chi^2t_+ + \frac{t_-^2}{3} \right)}{64\pi(s - m_e^2)^2} \frac{1}{\Lambda^4}, \quad (5.4b)$$

$$\sigma_{e\nu}^V = \frac{t_- \left\{ t_+^2 + 2(2s - m_\chi^2)t_+ + 8[(s - m_e^2)^2 - m_\chi^2s] + \frac{t_-^2}{3} \right\}}{32\pi(s - m_e^2)^2} \frac{1}{\Lambda^4}, \quad (5.4c)$$

$$\sigma_{e\nu}^A = \frac{t_- \left\{ t_+^2 + 2(2s - 4m_e^2 - m_\chi^2)t_+ + 8[(s - m_e^2)^2 - m_\chi^2(s - 2m_e^2)] + \frac{t_-^2}{3} \right\}}{32\pi(s - m_e^2)^2} \frac{1}{\Lambda^4}, \quad (5.4d)$$

$$\sigma_{e\nu}^T = \frac{t_- \left\{ t_+^2 + 2(4s - 2m_e^2 - m_\chi^2)t_+ + 8[2(s - m_e^2)^2 - m_\chi^2(2s - m_e^2)] + \frac{t_-^2}{3} \right\}}{8\pi(s - m_e^2)^2} \frac{1}{\Lambda^4}, \quad (5.4e)$$

with

$$t_- \equiv \frac{(s - m_e^2)\sqrt{(s - m_\chi^2 - m_e^2)^2 - 4m_\chi^2m_e^2}}{s}, \quad t_+ \equiv -\frac{(s - m_e^2)^2 - (s + m_e^2)m_\chi^2}{s}. \quad (5.5)$$

The generated DM yield can be converted into the DM relic density, $\Omega_\chi = 2m_\chi Y(T_0)s(T_0)/\rho_c$, with ρ_c being the critical density in the current Universe. Note that the overall factor 2 accounts for the identical contributions from χ and $\bar{\chi}$. Since the amount of DM has already been measured quite precisely, the DM relic density must not exceed the observed value $\Omega_{\text{dm}}h^2 \approx 0.12$ [103]. This DM overproduction requirement puts stringent constraint on the coupling strength. In Fig. 17, the dashed magenta line reproduces the constraint with only the s -channel e^+e^- annihilation while the new constraint with also the t -channel $e^\pm\nu$ scattering is given in the magenta filled region. Including the t -channel contribution improves the constraint by almost an order of magnitude. The t -channel contribution cannot be ignored.

5.2. DM Decay and Astrophysical X/γ Ray Observations

In the presence of coupling with charged electron and neutrino, the DM can decay into light SM particles including not just the massless photon and neutrinos but also electron and positron if the DM is heavy enough, $m_\chi > 2m_e$. We provide updated calculation and constraints for this heavy DM region. Due to space limitation, only results for the vector case are shown in Fig. 17 and our discussions below focus on this particular case.

$\chi \rightarrow \nu\nu\nu$: For DM mass $m_\chi \lesssim 2m_e$, the dominant decay mode is the invisible channel $\chi \rightarrow \nu\nu\nu$. Since neutrinos are relativistic degrees of freedom, the DM decay in the early Universe will inject radiative energy to influence the cosmic evolution. The constraint is obtained in [75] and extended above $2m_e$ to 1 GeV as the dashed brown line in Fig. 17. Although the branching ratio of this channel becomes suppressed in the presence of a new channel $\chi \rightarrow e^+e^-\nu$ for $m_\chi > 2m_e$, the cosmological expansion is sensitive to the decay width instead and hence the extension of the constraint curve is smoothly extended.

$\chi \rightarrow \nu\gamma\gamma\gamma$: For the vector operator with DM mass $m_\chi \lesssim 2m_e$, the dominant visible decay mode is the four-body channel $\chi \rightarrow \nu\gamma\gamma\gamma$. The constraint is shown as blue solid and dashed lines with division at $m_\chi = 2m_e$ using the same observational data summarized in [75]. It is obtained by requiring that the predicted photon flux from galactic and/or extragalactic DM decay does not exceed the diffuse X/ γ -ray background collected by the astrophysical observations (Insight-HXMT, NuSTAR, HEAO-1, and INTEGRAL). We can see the scaling behaviors with m_χ below and above $2m_e$ are quite different. For the light DM case, $\Gamma_{\chi \rightarrow \nu\gamma\gamma\gamma} \propto m_\chi^{13}/m_e^8\Lambda^4$ [75] while for the heavy one $\Gamma_{\chi \rightarrow \nu\gamma\gamma\gamma} \propto m_\chi^5/\Lambda^4$. On the other hand, the vertical axis variable scales as $\sigma_{\chi e}v_\chi \propto m_\chi^2/\Lambda^4$. Putting things together, $\sigma_{\chi e}v_\chi \propto m_\chi^{-11}(m_\chi^{-3})$ for $m_\chi \ll 2m_e$ ($m_\chi \gg 2m_e$), respectively. That is why the blue curve has much larger slope for light DM.

$\chi \rightarrow \nu e^+e^-$: For the DM mass beyond the electron-positron pair production threshold, $m_\chi > 2m_e$, the dominant visible decay mode is $\chi \rightarrow \nu e^+e^-$. The decay width of $\chi \rightarrow \nu e^+e^-$ due to the vector operator \mathcal{O}_V takes the form as,

$$\Gamma_{\chi \rightarrow \nu ee}^V = \frac{m_\chi^5}{6144\pi^3\Lambda^4} \left[(16 - 40\eta + 18\eta^2 - 9\eta^3)\sqrt{1-\eta} + 3(8 - 3\eta)\eta^3 \tanh^{-1}(\sqrt{1-\eta}) \right], \quad (5.6)$$

where $\eta \equiv 4m_e^2/m_\chi^2$. Requiring stable DM on the cosmological time scale, with a DM lifetime τ_χ larger than the age of the Universe, $\tau_\chi \approx 1/\Gamma_{\chi \rightarrow \nu ee} > 13.8$ Gyr, puts a conservative constraint as shown with the solid green line in Fig. 17. Even though the $\chi \rightarrow \nu e^+e^-$ channel dominates over $\chi \rightarrow \nu\gamma\gamma\gamma$, this constraint is still weaker by an order of magnitude or so.

For completeness, we also list the $\chi \rightarrow \nu ee$ decay width with $m_\chi \geq 2m_e$ from other operators,

$$\begin{aligned} \Gamma_{\chi \rightarrow \nu ee}^S &= \frac{m_\chi^5}{24576\pi^3\Lambda^4} \left[(16 - 88\eta - 42\eta^2 + 9\eta^3)\sqrt{1-\eta} + 3(48 - 16\eta + 3\eta^2)\eta^2 \tanh^{-1}(\sqrt{1-\eta}) \right], \\ \Gamma_{\chi \rightarrow \nu ee}^P &= \frac{m_\chi^5}{3072\pi^3\Lambda^4} \left[-5(2 - \eta) + (16 - 16\eta + 5\eta^2)\eta^2 {}_2F_1\left(\frac{3}{2}, 3; \frac{5}{2}; 1 - \eta\right) \right] (1 - \eta)^{\frac{3}{2}}, \\ \Gamma_{\chi \rightarrow \nu ee}^A &= \frac{m_\chi^5}{6144\pi^3\Lambda^4} \left[(16 - 72\eta - 22\eta^2 + 3\eta^3)\sqrt{1-\eta} + 3(32 - 8\eta + \eta^2)\eta^2 \tanh^{-1}(\sqrt{1-\eta}) \right], \\ \Gamma_{\chi \rightarrow \nu ee}^T &= \frac{m_\chi^5}{1024\pi^3\Lambda^4} \left[(16 - 56\eta - 2\eta^2 - 3\eta^3)\sqrt{1-\eta} + 3(16 - \eta^2)\eta^2 \tanh^{-1}(\sqrt{1-\eta}) \right], \end{aligned} \quad (5.7)$$

where ${}_2F_1(a, b; c; z)$ is the hypergeometric function. A factor of 2 is included to account for both neutrino and anti-neutrino final states. Other visible and invisible decay modes have been explored in our previous work [75]. For scalar, pseudo-scalar, and axial-vector operators, similar

to Fig. 17, the collider searches are also sensitive to light DM while the DM overproduction and decay constraints are stronger for the heavy counterpart. However, for the tensor case, the collider search is always worse than the DM visible decay mode $\chi \rightarrow \nu\gamma$ due to its large decay width.

For dark fermion with $m_\chi \gg 2m_e$, we can estimate the dark fermion lifetime from the vector-type operator,

$$\tau_\chi^V \approx \Gamma_{\chi\nu ee}^{V,-1} \approx \left(\frac{m_\chi^5}{384\pi^3\Lambda^4} \right)^{-1} = 7.83 \times 10^{-19} \text{ s} \left(\frac{\Lambda}{1 \text{ TeV}} \right)^4 \left(\frac{100 \text{ GeV}}{m_\chi} \right)^5, \quad (5.8)$$

from which the others are simple scalings, $\tau_\chi^{(S,P,A,T)} \approx (4, 4, 1, 1/6)\tau_\chi^V$. With strong boost effect for an energetic particle produced at collider, the decay length scales as,

$$L_\chi^V \approx 2.349 \times 10^{-10} \text{ m} \times \frac{1}{2} \frac{\sqrt{s}}{m_\chi} \left(1 + \frac{m_\chi^2}{s} \right) \left(\frac{\Lambda}{1 \text{ TeV}} \right)^4 \left(\frac{100 \text{ GeV}}{m_\chi} \right)^5. \quad (5.9)$$

It can reach $L_\chi^V \sim 10^{-4} \text{ m}$ at CEPC for $m_\chi = 10 \text{ GeV}$ and $\Lambda = 1 \text{ TeV}$. In other words, a heavy dark fermion can decay inside the detector and with a displaced vertex for $\mathcal{O}(\text{GeV})$ masses. But sub-GeV dark fermions contribute as missing energy. So more information can be extracted from its decay products to obtain even stronger constraint on the relevant absorption operators for at least GeV dark fermions. To be conservative, we only consider the missing energy search and leave more detailed studies for further study.

5.3. Direct Detection

The direct detection experiments are sensitive to the sub-MeV scale DM that leaves $\mathcal{O}(10) \text{ keV}$ electron recoil. We use XENON1T [104], PandaX-II [105], PandaX-4T [79], LZ [106], and XENONnT [107] to give an updated constraint. In addition to the fermionic DM absorption signal, the background estimations are also taken into consideration with a nuisance parameter [108]. Using the analytical χ^2 analysis [75, 109, 110], we obtain the 95% C.L. sensitivity curves/contours for XENON1T (gray), PandaX-II (green), PandaX-4T (blue), LZ (orange), and XENONnT (black) as shown in Fig. 17. While XENON1T and PandaX-4T give contours, the results from PandaX-II, LZ, and XENONnT are exclusion limits at 95% C.L.

6. Discussions and Conclusions

The collider searches can probe not just the genuine DM but also other dark sector particles. We focus on the absorption operators that couple a dark fermion with neutrino and the charged electron/positron. Although such operators have been highly constrained by the cosmological and astrophysical observations as systematically explored in our previous phenomenological paper [75], the future e^+e^- colliders can provide even better sensitivities particularly in the

sub-MeV mass range. The future lepton colliders (CEPC, ILC, and CLIC) can even surpass the current DM direct detection experiments (PandaX and XENON1T). In other words, the fermionic absorption DM is of great interest to not just the direct detection but also the collider search. While the indirect detection prevails for heavy DM and the direct detection for the keV scale, the collider search dominates at the light mass range and is hence of great advantage. So the three independent searches are still complementary to each other for the absorption operator scenario. Comparable feature happens for the cosmological limits from the DM overproduction requirement but the sensitivity is much weaker than the collider one.

Acknowledgements

SFG and KM would like to thank Ning Zhou, Hai-Jun Yang, and Manqi Ruan for useful discussions. The authors are supported by the National Natural Science Foundation of China (12090060, 12090064, 12375101, and 12305110) and the SJTU Double First Class start-up fund (WF220442604). SFG is also an affiliate member of Kavli IPMU, University of Tokyo. KM is supported by the Innovation Capability Support Program of Shaanxi (Program No. 2021KJXX-47). XDM is also supported by Guangdong Major Project of Basic and Applied Basic Research (No. 2020B0301030008).

References

- [1] G. Bertone, D. Hooper and J. Silk, “*Particle dark matter: Evidence, candidates and constraints*,” *Phys. Rept.* **405**, 279-390 (2005) [[arXiv:hep-ph/0404175](#) [hep-ph]].
- [2] B. L. Young, “*A survey of dark matter and related topics in cosmology*,” *Front. Phys. (Beijing)* **12**, no.2, 121201 (2017).
- [3] A. Arbey and F. Mahmoudi, “*Dark matter and the early Universe: a review*,” *Prog. Part. Nucl. Phys.* **119**, 103865 (2021) [[arXiv:2104.11488](#) [hep-ph]].
- [4] L. Roszkowski, E. M. Sessolo and S. Trojanowski, “*WIMP dark matter candidates and searches—current status and future prospects*,” *Rept. Prog. Phys.* **81**, no.6, 066201 (2018) [[arXiv:1707.06277](#) [hep-ph]].
- [5] M. Valluri, S. Chabanier, V. Irsic, E. Armengaud, M. Walther, C. Rockosi, M. A. Sanchez-Conde, L. B. Silva, A. P. Cooper and E. Darragh-Ford, *et al.* “*Snowmass2021 Cosmic Frontier White Paper: Prospects for obtaining Dark Matter Constraints with DESI*,” [[arXiv:2203.07491](#) [astro-ph.CO]].
- [6] J. Liu, X. Chen and X. Ji, “*Current status of direct dark matter detection experiments*,” *Nature Phys.* **13**, no.3, 212-216 (2017) [[arXiv:1709.00688](#) [astro-ph.CO]].

- [7] M. Schumann, “*Direct Detection of WIMP Dark Matter: Concepts and Status*,” *J. Phys. G* **46**, no.10, 103003 (2019) [[arXiv:1903.03026](#) [astro-ph.CO]].
- [8] J. Billard, M. Boulay, S. Cebrián, L. Covi, G. Fiorillo, A. Green, J. Kopp, B. Majorovits, K. Palladino and F. Petricca, *et al.* “*Direct detection of dark matter—APPEC committee report**,” *Rept. Prog. Phys.* **85**, no.5, 056201 (2022) [[arXiv:2104.07634](#) [hep-ex]].
- [9] J. M. Gaskins, “*A review of indirect searches for particle dark matter*,” *Contemp. Phys.* **57**, no.4, 496-525 (2016) [[arXiv:1604.00014](#) [astro-ph.HE]].
- [10] R. K. Leane, “*Indirect Detection of Dark Matter in the Galaxy*,” [[arXiv:2006.00513](#) [hep-ph]].
- [11] T. R. Slatyer, “*Les Houches Lectures on Indirect Detection of Dark Matter*,” *SciPost Phys. Lect. Notes* **53**, 1 (2022) [[arXiv:2109.02696](#) [hep-ph]].
- [12] A. Boveia and C. Doglioni, “*Dark Matter Searches at Colliders*,” *Ann. Rev. Nucl. Part. Sci.* **68**, 429-459 (2018) [[arXiv:1810.12238](#) [hep-ex]].
- [13] S. Gori, M. Williams, P. Ilten, N. Tran, G. Krnjaic, N. Toro, B. Batell, N. Blinov, C. Hearty and R. McGehee, *et al.* “*Dark Sector Physics at High-Intensity Experiments*,” [[arXiv:2209.04671](#) [hep-ph]].
- [14] T. Lagouri, “*Review on Higgs Hidden–Dark Sector Physics at High-Energy Colliders*,” *Symmetry* **14**, no.7, 1299 (2022).
- [15] B. Penning, “*The pursuit of dark matter at colliders—an overview*,” *J. Phys. G* **45**, no.6, 063001 (2018) [[arXiv:1712.01391](#) [hep-ex]].
- [16] S. Bottaro, D. Buttazzo, M. Costa, R. Franceschini, P. Panci, D. Redigolo and L. Vittorio, “*Closing the window on WIMP Dark Matter*,” *Eur. Phys. J. C* **82**, no.1, 31 (2022) [[arXiv:2107.09688](#) [hep-ph]].
- [17] G. Bertone and T. Tait, M.P., “*A new era in the search for dark matter*,” *Nature* **562**, no.7725, 51-56 (2018) [[arXiv:1810.01668](#) [astro-ph.CO]].
- [18] E. A. Baltz and L. Bergstrom, “*Detection of leptonic dark matter*,” *Phys. Rev. D* **67**, 043516 (2003) [[arXiv:hep-ph/0211325](#) [hep-ph]].
- [19] I. John and T. Linden, “*Cosmic-Ray Positrons Strongly Constrain Leptophilic Dark Matter*,” *JCAP* **12** (2021), 007 [[arXiv:2107.10261](#) [astro-ph.HE]].
- [20] X. J. Bi, X. G. He and Q. Yuan, “*Parameters in a class of leptophilic models from PAMELA, ATIC and FERMI*,” *Phys. Lett. B* **678**, 168-173 (2009) [[arXiv:0903.0122](#) [hep-ph]].
- [21] A. Ibarra, A. Ringwald, D. Tran and C. Weniger, “*Cosmic Rays from Leptophilic Dark Matter Decay via Kinetic Mixing*,” *JCAP* **08**, 017 (2009) [[arXiv:0903.3625](#) [hep-ph]].

- [22] J. H. Davis, “*The Past and Future of Light Dark Matter Direct Detection*,” *Int. J. Mod. Phys. A* **30**, no.15, 1530038 (2015) [arXiv:1506.03924 [hep-ph]].
- [23] M. Drewes, T. Lasserre, A. Merle, S. Mertens, R. Adhikari, M. Agostini, N. A. Ky, T. Araki, M. Archidiacono and M. Bahr, *et al.* “*A White Paper on keV Sterile Neutrino Dark Matter*,” *JCAP* **01**, 025 (2017) [arXiv:1602.04816 [hep-ph]].
- [24] C. Kouvaris and J. Pradler, “*Probing sub-GeV Dark Matter with conventional detectors*,” *Phys. Rev. Lett.* **118**, no.3, 031803 (2017) [arXiv:1607.01789 [hep-ph]].
- [25] K. N. Abazajian, “*Sterile neutrinos in cosmology*,” *Phys. Rept.* **711-712**, 1-28 (2017) [arXiv:1705.01837 [hep-ph]].
- [26] A. Boyarsky, M. Drewes, T. Lasserre, S. Mertens and O. Ruchayskiy, “*Sterile neutrino Dark Matter*,” *Prog. Part. Nucl. Phys.* **104**, 1-45 (2019) [arXiv:1807.07938 [hep-ph]].
- [27] J. Kopp, “*Sterile neutrinos as dark matter candidates*,” *SciPost Phys. Lect. Notes* **36**, 1 (2022) [arXiv:2109.00767 [hep-ph]].
- [28] P. J. Fox and E. Poppitz, “*Leptophilic Dark Matter*,” *Phys. Rev. D* **79**, 083528 (2009) [arXiv:0811.0399 [hep-ph]].
- [29] Q. H. Cao, E. Ma and G. Shaughnessy, “*Dark Matter: The Leptonic Connection*,” *Phys. Lett. B* **673**, 152-155 (2009) [arXiv:0901.1334 [hep-ph]].
- [30] H. Davoudiasl, “*Dark Matter with Time-Varying Leptophilic Couplings*,” *Phys. Rev. D* **80**, 043502 (2009) [arXiv:0904.3103 [hep-ph]].
- [31] J. Kopp, V. Niro, T. Schwetz and J. Zupan, “*DAMA/LIBRA and leptonically interacting Dark Matter*,” *Phys. Rev. D* **80**, 083502 (2009) [arXiv:0907.3159 [hep-ph]].
- [32] T. Cohen and K. M. Zurek, “*Leptophilic Dark Matter from the Lepton Asymmetry*,” *Phys. Rev. Lett.* **104**, 101301 (2010) [arXiv:0909.2035 [hep-ph]].
- [33] E. J. Chun, J. C. Park and S. Scopel, “*Dirac gaugino as leptophilic dark matter*,” *JCAP* **02**, 015 (2010) [arXiv:0911.5273 [hep-ph]].
- [34] N. Haba, Y. Kajiyama, S. Matsumoto, H. Okada and K. Yoshioka, “*Universally Leptophilic Dark Matter From Non-Abelian Discrete Symmetry*,” *Phys. Lett. B* **695**, 476-481 (2011) [arXiv:1008.4777 [hep-ph]].
- [35] P. Ko and Y. Omura, “*Supersymmetric $U(1)_B \times U(1)_L$ model with leptophilic and leptophobic cold dark matters*,” *Phys. Lett. B* **701**, 363-366 (2011) [arXiv:1012.4679 [hep-ph]].
- [36] D. Schmidt, T. Schwetz and T. Toma, “*Direct Detection of Leptophilic Dark Matter in a Model with Radiative Neutrino Masses*,” *Phys. Rev. D* **85**, 073009 (2012) [arXiv:1201.0906 [hep-ph]].
- [37] M. Das and S. Mohanty, “*Leptophilic dark matter in gauged $L_\mu - L_\tau$ extension of MSSM*,” *Phys. Rev. D* **89**, no.2, 025004 (2014) [arXiv:1306.4505 [hep-ph]].

- [38] S. Chang, R. Edezhath, J. Hutchinson and M. Luty, “*Leptophilic Effective WIMPs*,” [Phys. Rev. D **90**, no.1, 015011 \(2014\) \[arXiv:1402.7358 \[hep-ph\]\]](#).
- [39] N. F. Bell, Y. Cai, R. K. Leane and A. D. Medina, “*Leptophilic dark matter with Z' interactions*,” [Phys. Rev. D **90**, no.3, 035027 \(2014\) \[arXiv:1407.3001 \[hep-ph\]\]](#).
- [40] Q. H. Cao, C. R. Chen and T. Gong, “*Leptophilic dark matter confronts AMS-02 cosmic-ray positron flux*,” [Chin. J. Phys. **55**, 10-15 \(2017\) \[arXiv:1409.7317 \[hep-ph\]\]](#).
- [41] W. Chao, H. K. Guo, H. L. Li and J. Shu, “*Electron Flavored Dark Matter*,” [Phys. Lett. B **782**, 517-522 \(2018\) \[arXiv:1712.00037 \[hep-ph\]\]](#).
- [42] K. Ghorbani and P. H. Ghorbani, “*DAMPE electron-positron excess in leptophilic Z' model*,” [JHEP **05**, 125 \(2018\) \[arXiv:1712.01239 \[hep-ph\]\]](#).
- [43] Z. L. Han, W. Wang and R. Ding, “*Radiative Seesaw Model and DAMPE Excess from Leptophilic Gauge Symmetry*,” [Eur. Phys. J. C **78**, no.3, 216 \(2018\) \[arXiv:1712.05722 \[hep-ph\]\]](#).
- [44] E. Madge and P. Schwaller, “*Leptophilic dark matter from gauged lepton number: Phenomenology and gravitational wave signatures*,” [JHEP **02**, 048 \(2019\) \[arXiv:1809.09110 \[hep-ph\]\]](#).
- [45] S. I. Horigome, T. Katayose, S. Matsumoto and I. Saha, “*Leptophilic fermion WIMP: Role of future lepton colliders*,” [Phys. Rev. D **104**, no.5, 055001 \(2021\) \[arXiv:2102.08645 \[hep-ph\]\]](#).
- [46] S. Ghosh, A. Dutta Banik, E. J. Chun and D. Majumdar, “*Leptophilic-portal dark matter in the light of AMS-02 positron excess*,” [Phys. Rev. D **104**, no.7, 075016 \(2021\) \[arXiv:2003.07675 \[hep-ph\]\]](#).
- [47] S. Kundu, A. Guha, P. K. Das and P. S. B. Dev, “*EFT analysis of leptophilic dark matter at future electron-positron colliders in the mono-photon and mono- Z channels*,” [Phys. Rev. D **107**, no.1, 015003 \(2023\) \[arXiv:2110.06903 \[hep-ph\]\]](#).
- [48] B. Barman, S. Bhattacharya, S. Girmohanta and S. Jahedi, “*Effective Leptophilic WIMPs at the e^+e^- collider*,” [JHEP **04**, 146 \(2022\) \[arXiv:2109.10936 \[hep-ph\]\]](#).
- [49] J. Liang, Z. Liu and L. Yang, “*Probing sub-GeV leptophilic dark matter at Belle II and NA64*,” [JHEP **05**, 184 \(2022\) \[arXiv:2111.15533 \[hep-ph\]\]](#).
- [50] F. del Aguila, M. Chala, J. Santiago and Y. Yamamoto, “*Collider limits on leptophilic interactions*,” [JHEP **03**, 059 \(2015\) \[arXiv:1411.7394 \[hep-ph\]\]](#).
- [51] M. R. Buckley and D. Feld, “*Dark Matter in Leptophilic Higgs Models After the LHC Run-I*,” [Phys. Rev. D **92**, no.7, 075024 \(2015\) \[arXiv:1508.00908 \[hep-ph\]\]](#).

- [52] Y. Farzan, S. Pascoli and M. A. Schmidt, “*AMEND: A model explaining neutrino masses and dark matter testable at the LHC and MEG*,” *JHEP* **10**, 111 (2010) [[arXiv:1005.5323](#) [hep-ph]].
- [53] S. Su and B. Thomas, “*The LHC Discovery Potential of a Leptophilic Higgs*,” *Phys. Rev. D* **79**, 095014 (2009) [[arXiv:0903.0667](#) [hep-ph]].
- [54] F. Kahlhoefer, “*Review of LHC Dark Matter Searches*,” *Int. J. Mod. Phys. A* **32**, no.13, 1730006 (2017) [[arXiv:1702.02430](#) [hep-ph]].
- [55] C. Bartels, M. Berggren and J. List, “*Characterising WIMPs at a future e^+e^- Linear Collider*,” *Eur. Phys. J. C* **72**, 2213 (2012) [[arXiv:1206.6639](#) [hep-ex]].
- [56] A. Freitas and S. Westhoff, “*Leptophilic Dark Matter in Lepton Interactions at LEP and ILC*,” *JHEP* **10**, 116 (2014) [[arXiv:1408.1959](#) [hep-ph]].
- [57] H. Dreiner, M. Huck, M. Krämer, D. Schmeier and J. Tattersall, “*Illuminating Dark Matter at the ILC*,” *Phys. Rev. D* **87**, no.7, 075015 (2013) [[arXiv:1211.2254](#) [hep-ph]].
- [58] M. Habermehl, M. Berggren and J. List, “*WIMP Dark Matter at the International Linear Collider*,” *Phys. Rev. D* **101**, no.7, 075053 (2020) [[arXiv:2001.03011](#) [hep-ex]].
- [59] H. Bharadwaj and A. Goyal, “*Effective Field Theory approach to lepto-philic self conjugate dark matter*,” *Chin. Phys. C* **45**, no.2, 023114 (2021) [[arXiv:2008.13621](#) [hep-ph]].
- [60] J. Kalinowski, W. Kotlarski, K. Mekala, P. Sopicki and A. F. Zarnecki, “*Sensitivity of future linear e^+e^- colliders to processes of dark matter production with light mediator exchange*,” *Eur. Phys. J. C* **81**, no.10, 955 (2021) [[arXiv:2107.11194](#) [hep-ph]].
- [61] P. J. Fox, R. Harnik, J. Kopp and Y. Tsai, “*LEP Shines Light on Dark Matter*,” *Phys. Rev. D* **84**, 014028 (2011) [[arXiv:1103.0240](#) [hep-ph]].
- [62] Y. J. Chae and M. Perelstein, “*Dark Matter Search at a Linear Collider: Effective Operator Approach*,” *JHEP* **05**, 138 (2013) [[arXiv:1211.4008](#) [hep-ph]].
- [63] J. Abdallah *et al.* [DELPHI], “*Photon events with missing energy in e^+e^- collisions at $s^{*}(1/2) = 130\text{-GeV}$ to 209-GeV* ,” *Eur. Phys. J. C* **38**, 395-411 (2005) [[arXiv:hep-ex/0406019](#) [hep-ex]].
- [64] J. Abdallah *et al.* [DELPHI], “*Search for one large extra dimension with the DELPHI detector at LEP*,” *Eur. Phys. J. C* **60**, 17-23 (2009) [[arXiv:0901.4486](#) [hep-ex]].
- [65] A. Birkedal, K. Matchev and M. Perelstein, “*Dark matter at colliders: A Model independent approach*,” *Phys. Rev. D* **70**, 077701 (2004) [[arXiv:hep-ph/0403004](#) [hep-ph]].
- [66] Z. Liu, Y. H. Xu and Y. Zhang, “*Probing dark matter particles at CEPC*,” *JHEP* **06**, 009 (2019) [[arXiv:1903.12114](#) [hep-ph]].

- [67] N. Wan, M. Song, G. Li, W. G. Ma, R. Y. Zhang and J. Y. Guo, “*Searching for dark matter via mono-Z boson production at the ILC*,” *Eur. Phys. J. C* **74**, no.12, 3219 (2014) [[arXiv:1403.7921](#) [hep-ph]].
- [68] Z. H. Yu, X. J. Bi, Q. S. Yan and P. F. Yin, “*Dark matter searches in the mono-Z channel at high energy e^+e^- colliders*,” *Phys. Rev. D* **90**, no.5, 055010 (2014) [[arXiv:1404.6990](#) [hep-ph]].
- [69] S. Dutta, D. Sachdeva and B. Rawat, “*Signals of Leptophilic Dark Matter at the ILC*,” *Eur. Phys. J. C* **77**, no.9, 639 (2017) [[arXiv:1704.03994](#) [hep-ph]].
- [70] B. Grzadkowski, M. Iglicki, K. Mekala and A. F. Zarnecki, “*Dark-matter-spin effects at future e^+e^- colliders*,” *JHEP* **08**, 052 (2020) [[arXiv:2003.06719](#) [hep-ph]].
- [71] A. Albert, M. Bauer, J. Brooke, O. Buchmueller, D. G. Cerdeño, M. Citron, G. Davies, A. De Cosa, A. De Roeck and A. De Simone, *et al.* “*Towards the next generation of simplified Dark Matter models*,” *Phys. Dark Univ.* **16**, 49-70 (2017) [[arXiv:1607.06680](#) [hep-ex]].
- [72] K. Arun, S. B. Gudennavar and C. Sivaram, “*Dark matter, dark energy, and alternate models: A review*,” *Adv. Space Res.* **60**, 166-186 (2017) [[arXiv:1704.06155](#) [physics.gen-ph]].
- [73] T. Lin, “*Dark matter models and direct detection*,” *PoS* **333**, 009 (2019) [[arXiv:1904.07915](#) [hep-ph]].
- [74] C. R. Chen and F. Takahashi, “*Cosmic rays from Leptonic Dark Matter*,” *JCAP* **02**, 004 (2009) [[arXiv:0810.4110](#) [hep-ph]].
- [75] Shao-Feng Ge, Xiao-Gang He, Xiao-Dong Ma and Jie Sheng, “*Revisiting the fermionic dark matter absorption on electron target*,” *JHEP* **05**, 191 (2022) [[arXiv:2201.11497](#) [hep-ph]].
- [76] J. F. Nieves and P. B. Pal, “*Generalized Fierz identities*,” *Am. J. Phys.* **72**, 1100-1108 (2004) [[arXiv:hep-ph/0306087](#) [hep-ph]].
- [77] C. C. Nishi, “*Simple derivation of general Fierz-like identities*,” *Am. J. Phys.* **73**, 1160-1163 (2005) [[arXiv:hep-ph/0412245](#) [hep-ph]].
- [78] Y. Liao and J. Y. Liu, “*Generalized Fierz Identities and Applications to Spin-3/2 Particles*,” *Eur. Phys. J. Plus* **127**, 121 (2012) [[arXiv:1206.5141](#) [hep-ph]].
- [79] D. Zhang *et al.* [PandaX], Shao-Feng Ge, Xiao-Gang He, Xiao-Dong Ma, and Jie Sheng, “*Search for Light Fermionic Dark Matter Absorption on Electrons in PandaX-4T*,” *Phys. Rev. Lett.* **129**, no.16, 161804 (2022) [[arXiv:2206.02339](#) [hep-ex]].
- [80] K. Ma, “*Mono- γ Production of a Vector Dark Matter at Future e^+e^- Collider*,” *Chin. Phys. C* **46**, no.11, 113104 (2022) [[arXiv:2205.05560](#) [hep-ph]].

- [81] J. Alwall, R. Frederix, S. Frixione, V. Hirschi, F. Maltoni, O. Mattelaer, H. S. Shao, T. Stelzer, P. Torrielli and M. Zaro, “*The automated computation of tree-level and next-to-leading order differential cross sections, and their matching to parton shower simulations*,” *JHEP* **07**, 079 (2014) [[arXiv:1405.0301](#) [hep-ph]].
- [82] A. Alloul, N. D. Christensen, C. Degrande, C. Duhr and B. Fuks, “*FeynRules 2.0 - A complete toolbox for tree-level phenomenology*,” *Comput. Phys. Commun.* **185**, 2250-2300 (2014) [[arXiv:1310.1921](#) [hep-ph]].
- [83] F. A. Berends and R. Kleiss, “*Distributions in the Process $e^+ e^- \rightarrow e^+ e^- (\text{Gamma})$* ,” *Nucl. Phys. B* **228**, 537-551 (1983).
- [84] K. Tobimatsu and Y. Shimizu, “*Radiative Correction to $e^+ e^- \rightarrow e^+ e^-$ in the Electroweak Theory. 1. Cross-sections for Hard Photon Emission*,” *Prog. Theor. Phys.* **74**, 567 (1985) [erratum: *Prog. Theor. Phys.* **76**, 334 (1986)].
- [85] M. Habermehl, “*Dark Matter at the International Linear Collider*,” [DESY-THESIS-2018-039](#).
- [86] J. B. Guimarães da Costa *et al.* [CEPC Study Group], “*CEPC Conceptual Design Report: Volume 2 - Physics & Detector*,” [[arXiv:1811.10545](#) [hep-ex]].
- [87] A. Abada *et al.* [FCC], “*FCC-ee: The Lepton Collider: Future Circular Collider Conceptual Design Report Volume 2*,” *Eur. Phys. J. ST* **228**, no.2, 261-623 (2019)
- [88] A. Abada *et al.* [FCC], “*FCC Physics Opportunities: Future Circular Collider Conceptual Design Report Volume 1*,” *Eur. Phys. J. C* **79**, no.6, 474 (2019)
- [89] P. Bambade, T. Barklow, T. Behnke, M. Berggren, J. Brau, P. Burrows, D. Denisov, A. Faus-Golfe, B. Foster and K. Fujii, *et al.*, “*The International Linear Collider: A Global Project*,” [[arXiv:1903.01629](#) [hep-ex]].
- [90] T. Barklow, J. Brau, K. Fujii, J. Gao, J. List, N. Walker and K. Yokoya, “*ILC Operating Scenarios*,” [[arXiv:1506.07830](#) [hep-ex]].
- [91] M. Aicheler *et al.* [CLIC accelerator], “*The Compact Linear Collider (CLIC) - Project Implementation Plan*,” *CERN Yellow Reports: Monographs*, **4**, (2018) [[arXiv:1903.08655](#) [physics.acc-ph]].
- [92] Z. Duan, J. Gao, X. Li, D. Wang, Y. Wang, W. Xia, Q. Xu, C. Yu and Y. Zhang, “*Concepts of Longitudinally Polarized Electron and Positron Colliding Beams in the Circular Electron Positron Collider*,” [JACoW-IPAC2019-MOPMP012](#)
- [93] Z. Duan, T. Chen, J. Gao, D. Ji, X. Li, D. Wang, J. Wang, Y. Wang and W. Xia, “*Longitudinally Polarized Colliding Beams at the CEPC*,” *JACoW eeFACT2022* (2023), [97-102](#)
- [94] S. R. Mane, “*Polarization at TLEP/FCC-ee: ideas and estimates*,” [[arXiv:1406.0561](#) [physics.acc-ph]].

- [95] A. Blondel, P. Janot, J. Wenninger, R. Aßmann, S. Aumon, P. Azzurri, D. P. Barber, M. Benedikt, A. V. Bogomyagkov and E. Gianfelice-Wendt, *et al.* “Polarization and Centre-of-mass Energy Calibration at FCC-ee,” [[arXiv:1909.12245](#) [physics.acc-ph]].
- [96] A. Blondel and E. Gianfelice, “The challenges of beam polarization and keV-scale centre-of-mass energy calibration at the FCC-ee,” *Eur. Phys. J. Plus* **136**, no.11, 1103 (2021).
- [97] K. Fujii, C. Grojean, M. E. Peskin, T. Barklow, Y. Gao, S. Kanemura, H. Kim, J. List, M. Nojiri and M. Perelstein, “Physics Case for the 250 GeV Stage of the International Linear Collider,” *CERN Yellow Reports: Monographs*, **4**, (2018) [[arXiv:1710.07621](#) [hep-ex]].
- [98] C. Chen, Z. Cui, G. Li, Q. Li, M. Ruan, L. Wang and Q. s. Yan, “ $H \rightarrow e^+e^-$ at CEPC: ISR effect with MadGraph,” [[arXiv:1705.04486](#) [hep-ph]].
- [99] Q. Li and Q. S. Yan, “Initial State Radiation Simulation with MadGraph,” [[arXiv:1804.00125](#) [hep-ph]].
- [100] J. J. Blaising *et al.* [CLICdp], “Physics performance for Dark Matter searches at $\sqrt{s} = 3$ TeV at CLIC using mono-photons and polarised beams,” [[arXiv:2103.06006](#) [hep-ex]].
- [101] E. Boos *et al.* [CompHEP], “CompHEP 4.4: Automatic computations from Lagrangians to events,” *Nucl. Instrum. Meth. A* **534**, 250-259 (2004) [[arXiv:hep-ph/0403113](#) [hep-ph]].
- [102] A. Belyaev, N. D. Christensen and A. Pukhov, “CalcHEP 3.4 for collider physics within and beyond the Standard Model,” *Comput. Phys. Commun.* **184**, 1729-1769 (2013) [[arXiv:1207.6082](#) [hep-ph]].
- [103] N. Aghanim *et al.* [Planck], “Planck 2018 results. VI. Cosmological parameters,” *Astron. Astrophys.* **641**, A6 (2020) [erratum: *Astron. Astrophys.* **652**, C4 (2021)] [[arXiv:1807.06209](#) [astro-ph.CO]].
- [104] E. Aprile *et al.* [XENON], “Excess electronic recoil events in XENON1T,” *Phys. Rev. D* **102**, no.7, 072004 (2020) [[arXiv:2006.09721](#) [hep-ex]].
- [105] X. Zhou *et al.* [PandaX-II], “A Search for Solar Axions and Anomalous Neutrino Magnetic Moment with the Complete PandaX-II Data,” *Chin. Phys. Lett.* **38**, no.1, 011301 (2021) [[arXiv:2008.06485](#) [hep-ex]].
- [106] J. Aalbers *et al.* [LZ], “First Dark Matter Search Results from the LUX-ZEPLIN (LZ) Experiment,” [[arXiv:2207.03764](#) [hep-ex]].
- [107] E. Aprile *et al.* [XENON], “Search for New Physics in Electronic Recoil Data from XENONnT,” *Phys. Rev. Lett.* **129**, no.16, 161805 (2022) [[arXiv:2207.11330](#) [hep-ex]].
- [108] Shao-Feng Ge, Pedro Pasquini, and Jie Sheng, “Solar active-sterile neutrino conversion with atomic effects at dark matter direct detection experiments,” *JHEP* **05**, 088 (2022) [[arXiv:2112.05560](#) [hep-ph]].

- [109] Shao-Feng Ge, Kauru Hagiwara, N. Okamura and Y. Takaesu, “*Determination of mass hierarchy with medium baseline reactor neutrino experiments*,” [JHEP **05**, 131 \(2013\)](#) [[arXiv:1210.8141](#) [hep-ph]].
- [110] Shao-Feng Ge, Hong-Jian He and Rui-Qing Xiao, “*Probing new physics scales from Higgs and electroweak observables at e^+e^- Higgs factory*,” [JHEP **10**, 007 \(2016\)](#) [[arXiv:1603.03385](#) [hep-ph]].
- [111] Massimo Casarsa, Marco Fabbrichesi, and Emidio Gabrielli “*Monochromatic single photon events at the muon collider*,” [Phys.Rev. **D 105**, 075008\(2022\)](#) [[arXiv:2111.13220](#) [hep-ph]].